Pulse Shaping for High Harmonic Generation

Johan Reinink

Master thesis
Applied Physics

University of Twente
Faculty of Science and Technology
& MESA+ Research Institute for Nanotechnology
Laser Physics and Nonlinear Optics

Supervisor:
Dr P.J.M van der Slot

Graduation committee:
Prof. dr. K.J. Boller
Dr P.J.M van der Slot
Dr. Ir. H.L. Offerhaus

This research is funded by STW (project number 10759).
Partners in the research are Coherent Europe B.V. and FERMI@Elettra.

Abstract

Extreme UltraViolet (EUV) radiation covers the spectral range from 124 nm down to 10 nm. This wavelength range is important for many applications, in particular next-generation lithography will use 13.5-nm light. One of the methods to generate coherent light in this wavelength region is high-harmonic generation, where a short (~35 fs), infra-red laser pulse is focused to high intensity in a capillary. The extremely nonlinear process that takes place in the capillary generated the EUV radiation. In this thesis we have investigated how the energy in the EUV can be increased, for all harmonics or a single particular harmonic.

To this end, the drive laser pulse energy is increased to about 7 mJ. Also, the drive laser system was modified to include a so-called Dazzler for shaping of the pulse it generates. Optimization of EUV generation through shaping of the drive laser pulse is also investigate. An evolutionary algorithm is used for the optimization. To keep the local intensity in the capillary constant, its diameter is also increased from 150 to 500 μm. The increase in total drive laser pulse energy also required modification to the diagnostic section; mainly it needed to be moved to a large distance from the capillary in order to safely separate the IR drive laser pulse from the generated EUV radiation

With the modified set-up we first characterized the EUV radiation generated by IR drive laser pulse with an energy in the range of 5 to 7.5 mJ and a duration of 35 fs when it propagates through the capillary filled with Argon. We observed a stable output pulse at low pressures (3 – 7 mbar) and found that the EUV oscillated in position primarily in the x-direction at higher pressures (up to 12 mbar) with increasing amplitude and frequency.

The measured spectrum showed that the harmonic orders from 15 to 29 can be generated and that the yield of a particular harmonic can be optimized by tuning the pressure (pressure phase matching). The range of harmonics found is slightly smaller than that found for a capillary with 150 μm diameter.

To investigate the effect of pulse shaping on the generation of EUV radiation, we used the Dazzler in combination with evolutionary algorithm to optimize the yield of a particular harmonic. An enhancement of a factor of 9.7 is obtained for the 23^{rd} harmonic compared to the same harmonic produced with the Dazzler in self-compensating mode (i.e., when the laser system is set to produces the shortest pulse. Only phase shaping is used. We also tried to optimize for red- or blue-shifted harmonics and observed a maximum shift of 0.11 nm.

Table of Contents

1 Introduction

Light is an invaluable tool for physicist to detect, analyze and manipulate matter on an ever-shrinking scale. This thesis focuses on the generation of EUV light; that is light in the spectral range from 124 down to 10 nm. Examples of the use of EUV light are the fundamental research done at Free-Electron Laser (FEL) facilities and the quest to manufacture the smallest features using lithography.

The EUV to hard x-rays produced by the FEL facilities allow for high-resolution microscopy down to the nm-level. The radiation can also be used for diffractive imaging and allows resolving the three-dimensional structure of complex structures such as proteins and viruses[1]. Unfortunately, most of these FEL facilities operate in the so-called self-amplified spontaneous emission regime that results in large short-to-shot fluctuations both in temporal shape and spectral content. Letting these systems start from a coherent seed signal would significantly improve the beam quality and greatly simplify experimental procedures. High-harmonic generation may function as a seed source for FELs.

High-harmonic generation (HHG) is an extremely nonlinear process generating extreme ultraviolet (EUV) radiation from a long wavelength radiation source. This allows wavelengths in the order of 1-100 nm to be generated from an infrared laser source that has a much longer wavelength, typically around 800 nm. The very high intensities required are in the order of 10^{14} W/cm^2 in a noble gas medium. At these intensities, the electric field significantly distorts the binding potential of the outer electron in a noble gas atom. This results in tunnel ionization of the electron followed by acceleration away from the parent ion. When the electric field of the drive laser reverses direction, the electron is driven back to its parent ion. When it recombines, the available energy is released in a short burst of radiation reaching into the EUV wavelength range. Further enhancement can be obtained through phase matching. This is the process of matching the propagation speed of the drive laser beam and one of the generated harmonics, resulting in a bright coherent beam. As the EUV generation occurs every half cycle of the laser only the odd harmonics will survive the resulting interference. The drive laser wavelength is fixed meaning that the wavelengths of the harmonics that are generated are fixed as well. To increase both the efficiency of a particular harmonic (selective enhancement) and tune a particular harmonic, shaping of the drive laser pulse can be used[2-4].

Pulse shaping is an area that opened up many possibilities of controlling processes with light such as selective 2 photon fluorescence[5], selectively breaking chemical bonds[6] and many more examples[7-9]. Shaping the drive laser pulse of the HHG setup can be used to achieve selective enhancement and tunability of the harmonics, effectively creating a light source with on demand specifications.

This thesis describes the work on generating high-harmonics in a large diameter capillary and on shaping for high harmonic generation. The remainder of this thesis is organized as followed. In chapter 2 a description is given of high harmonic generation at the atomic level using a simple semi-classical three-step model. The phase-matching condition is given for the macroscopic buildup, which describes the theory of the formation of a coherent beam from the contributions of

the atoms. A small insight in the theory of the influence of pulse shaping on the HHG process concludes this chapter. Chapter 3 focuses on the principles behind pulse shaping. The theory of Acousto-optic programmable dispersive filters (AOPDF) is treated to give insight in the working principle of the shaping method used in this thesis. Previous work and achieved results are discussed and the goals for the shaping experiments are set. In Chapter 4 a thorough description of the experimental setup and the design decisions made in the construction to achieve a stable and reliable HHG setup are given. This chapter discusses the various subsystems that make up the complete setup. The experimental results are presented in the chapter 5. This chapter covers the characterization of the setup as well as the results of the shaping experiments. Finally a discussion of the results is given in chapter 6, together with the conclusions and a outlook for improvements to the setup and future experiments.

2
HHG Theory

We first discuss the single atom response to the applied drive-laser field. The moment of ionization determines the subsequent electron trajectory and these trajectories play an important role in the effect that shaped drive-laser pulses have on the generation of high harmonics. We then discuss the phase-matching conditions that describe the conditions needed for coherent addition of radiation from the individual atoms. We follow the description given by Winterfeldt[10].

2.1 Single atom response

The single atom response can be described both semi-classically and quantum-mechanically. The semi-classical description is treated here as it is conceptually easier to understand. The semi-classical description consist of the so-called three-step model[11]. The three steps are ionization, acceleration of the electron and recombination. The three steps are schematically shown in figure 2.1. In this model the atom is simplified to one electron of the outer shell in a potential well created by the atom. Electron-electron interactions are neglected and the effects of the inner electrons and the core of the atom are simplified to a static Coulomb potential.

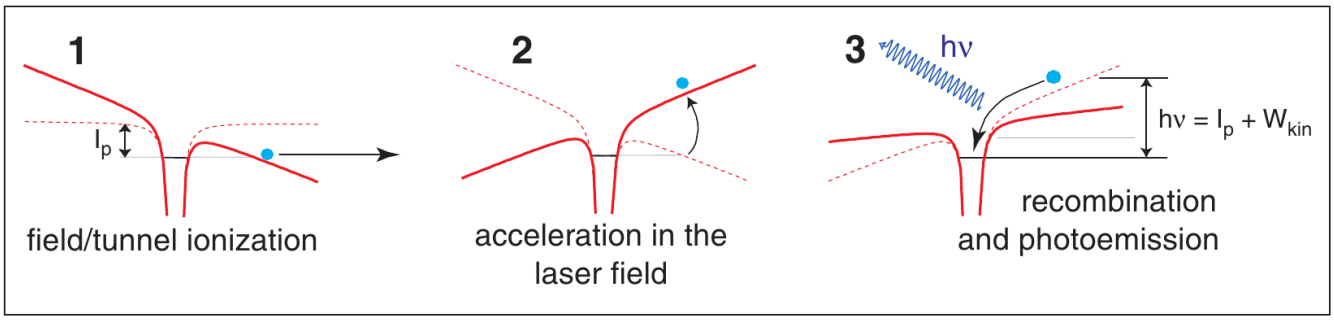

Figure 2.1: A schematic view of the three steps model. 1: Tunnel ionization by the drive laser field. 2: Acceleration in the drive laser field. 3: recombination with the parent ion and the emission of photons[10].

The drive laser is taken as a time varying potential. On an atomic scale the wavelength of the drive laser is large enough for the electric field to be approximated as homogeneous. The atomic potential in which the electron sits with no drive laser field applied is visible in figure 2.1 as a dotted line. Applying a drive laser field adds a linear potential to the potential of the atom itself. This is shown in figure 2.1 as a solid line.

The drive laser field lowers the potential barrier of the electron. The electron then can escape the potential well by tunnel ionization. The probability of ionization is inversely related to the width and height of the potential barrier. With no applied drive laser field the electron won't be able to escape the atom, while with an applied field equal to the strength of the barrier the atom will escape unhindered.

After the electron has escaped the atom it can be considered as a classical particle driven by the electric field of the drive laser. The moment of ionization is not fixed as the tunnel ionization has a certain probability to occur during each half cycle of the drive laser field. The electron is accelerated away from the parent ion it originated from during the remainder of the half cycle.

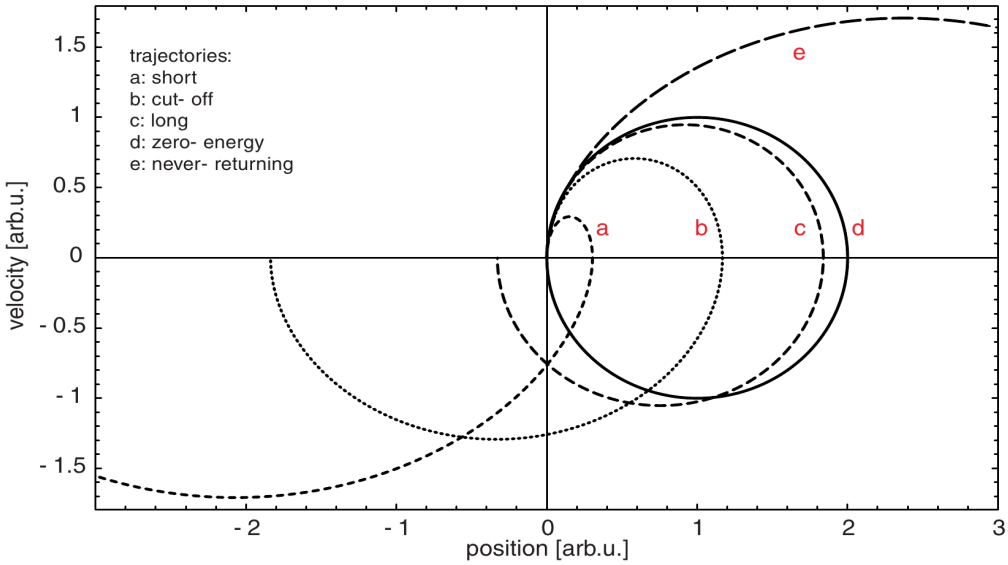

Figure 2.2: Different electron trajectories plotted in a velocity versus position graph. Each electron trajectory corresponds to a different moment of ionization. a: Short trajectory, late ionization (φ = 45 deg). b: cutoff trajectory, maximum kinetic energy. φ = 17deg. c: Long trajectory, early ionization (φ = 3deg). d: Starts at peak of electric field but returns with no kinetic energy (φ = 0deg). e: Never returns to parent ion (φ = -45deg)[10].

In the next half cycle the polarity of the drive laser field has flipped sign and the electron is pushed back towards the parent ion. The electron can make different trajectories depending on the moment of ionization during the half cycle of the drive laser field which is described by the phase φ of the drive laser field with φ=0 corresponding to the peak strength of the field. The different types of trajectories are plotted in figure 2.2. The electron is accelerated away from the ion to a positive position measured along the direction of polarization of the drive laser pulse. Recombination occurs when the position is again zero, i.e. when the electron trajectory intercepts the vertical axis in figure. The velocity at that moment determines the kinetic energy available upon recombination.
A late ionization will let the electron make a short trajectory (trajectory a) while an early ionization will make a long trajectory (trajectory c). The maximum kinetic energy at recombination is obtained at a phase of the drive laser field of 17 degrees (trajectory b). This trajectory is known as the cutoff trajectory. A very early ionization will drive the electron too far away from the parent ion for it to recombine in the next half cycle of the driver laser field.

Upon recombination the electron has gained kinetic energy from the acceleration by the drive laser field. The total energy available at recombination is the kinetic energy and the ionization potential. The highest energy harmonic is generated by electrons from the cutoff trajectory. The energy of this harmonic is given by:

$$E_{cut\text{-}off} = h\omega_{max} = I_p + E_{kin} = I_p + 3.17\,U_p \qquad 2.1$$

Where I_p is the ionization potential and E_{kin} = 3.17 U_p the maximum kinetic energy of the electron at recombination (trajectory b). U_p is the ponderomotive potential and is described by the following equation:

$$U_p = (e^2 E_L^2)/(4 m_e \omega_L^2) \propto I \lambda^2 \qquad 2.2$$

We can see from equation 2.2 that energy gained by the electron in the ponderomotive potential is proportional to the intensity of the drive laser and the drive laser wavelength squared. A long wavelength drive laser would give a higher cutoff energy but, due to the longer trajectory, would also have a lower the probability of recombination[12].

2.2 Phase matching

In the previous section the emission of high harmonics is considered for a single atom. In this section the macroscopic buildup from all individual emitters is treated. Since an EUV pulse is generated every half-cycle there are only odd harmonics generated. Breaking this symmetry can generate even harmonics. This can be done by using a two-color drive laser[13] or single-cycle drive laser pulses[14].

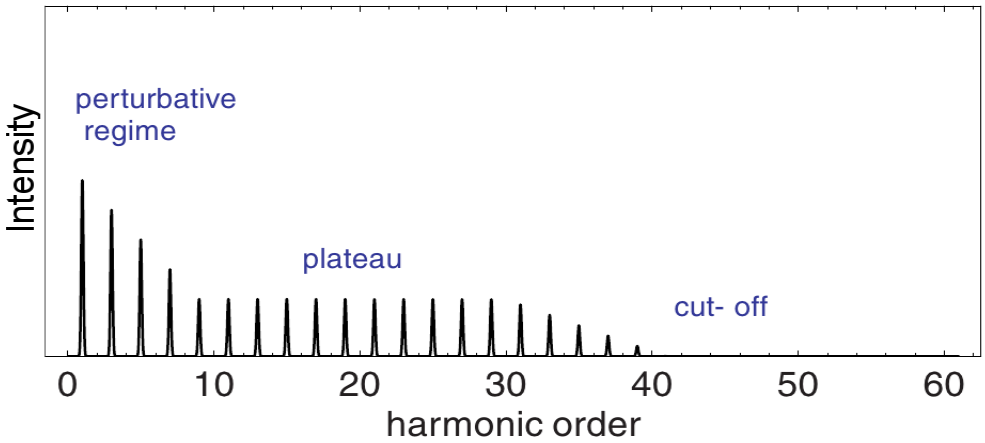

Figure 2.3: A typical high harmonic spectrum. Adapted from[10].

The spectrum of the high harmonics has a characteristic shape as seen in figure 2.3. The intensity of a harmonic drops until a plateau is reached. The harmonics in the plateau are constant in intensity. After the plateau the intensity drops of quickly at the cut-off frequency. The generated spectrum will also depend on phase matching, which limits the number of harmonics that are generated.

The goal of phase matching is to have all contributions of the individual atoms interfere constructively in the propagation direction of the drive laser. Both the drive laser pulse and the EUV pulse propagate through the capillary. The propagation speed of both need to be matched to allow constructive interfere of newly generated EUV with the previously generated EUV. Different propagation speeds will cause a phase difference to build up. After a phase shift of π the newly generated EUV light will interfere destructively. This limits the useful interaction length.

The EUV radiation has a short wavelength and experiences no guiding by the capillary, leaving only the dispersion of the noble gas. An ionized noble gas has a different dispersion than a neutral noble gas. This makes the dispersion and thus phase matching dependent on the ionization fraction. The phase matching is further dependent on the refractive index of the noble gas, which depends on the pressure. The k-vector for the EUV light can be written as:

$$k_{EUV} = 2\pi/\lambda_{EUV} + (2\pi N_a n(\lambda_{EUV}))/\lambda_{EUV} - N_e r_e \lambda_{EUV} \quad 2.3$$

where N_a is the density of neutral atoms, N_e the density of ionized atoms and r_e the classical electron radius. λ_{EUV} is the wavelength of the generated high harmonic. n*(λ)* is the refractive index minus one for the noble gas per unit neutral atom density at wavelength λ. The equation for the k-vector consists of a vacuum, neutral gas and plasma term. The contribution from the plasma is from its free electrons and is negative.
The drive laser is guided by the capillary. It experiences both the dispersion of the argon gas as well as the dispersion of the capillary mode. The k-vector for the drive laser is given by:

$$k = 2\pi/\lambda + (2\pi N_a n(\lambda))/\lambda - N_e r_e \lambda - (u_{nm}^2 \lambda)/(4\pi a^2) \quad 2.4$$

where u_{nm}, this is the m-th root of the Bessel function $J_{n-1}(z)$ for the waveguide and a is the inner radius of the capillary. For phase matching both k vectors need to match. The mismatch can be written as:

$$\Delta k_q = q k_{laser} - k_{EUV} \quad 2.5$$

Phase matching is achieved for $\Delta k_q = 0$. Rewriting the mismatch and taking $\lambda_{EUV} = \lambda / q$ gives:

$$\Delta k_q = q \frac{2\pi N_a}{\lambda} \cdot (n(\lambda) - n(\lambda/q)) + N_e r_e \lambda \left(\frac{1-q^2}{q} \right) - q \frac{u_{nm}^2 \lambda}{4\pi a^2} \quad 2.6$$

We can then introduce the pressure P in atmosphere, the atomic number density N_{atm} at atmospheric pressure and Δn, which is defined as the difference between the refractive indexes at atmospheric pressure of the neutral gas for the drive laser and EUV light. This rewrites to:

$$\Delta k_q = \frac{2\pi q}{\lambda} \cdot (1-\eta) P \Delta n - P \eta N_{atm} r_e \lambda \left(\frac{q^2-1}{q} \right) - \frac{u^{2nm} \lambda}{4\pi a^2} \cdot \left(\frac{q^2-1}{q} \right) \quad 2.7$$

The contributions of the plasma and the waveguide are negative while the remaining contributions are positive. This allows the phase matching condition to occur at the point where the negative terms cancel out the positive term.
The parameters that can be varied to achieve phase matching are the pressure, capillary radius and ionization fraction. In an experiment, for a given drive laser pulse propagating through the capillary, the pressure is fixed as well as the capillary diameter and the refractive index and atomic number density of the noble gas used. With a fixed ionization degree this would only allow a single harmonic to be phase matched. The ionization degree however varies with time as the drive laser pulse ionizes more atoms. This allows multiple harmonics to be phase matched after each other, giving rise to an output spectrum containing multiple harmonics.

3
Pulse shaping

In this chapter the different approaches to pulse shaping are discussed with a focus on the Acousto-optic programmable dispersive filter (AOPDF) as this is the shaping method used for the measurements in this thesis. This is followed by a brief discussion of previous work done on pulse shaping for HHG. The last section describes the goal of the shaping experiments done and covers the main motivation for this thesis.

3.1 Pulse shaping methods

Pulse shaping can be done in many ways. A basic understanding of the different pulse shaping approaches gives not only useful knowledge of the shaping process itself but also allows a better understanding and comparison with the results obtained with them. In the following, shaping with a spatial light modulator and with a deformable mirror will be briefly discussed before focusing on shaping with an AOPDF as the method used in this thesis.
The short duration of femtosecond laser pulses implies a wide bandwidth according to the Fourier theorem. Femtosecond pulses are most often the shortest event available. Temporal shaping would require the shaping mechanism to work at a shorter time scale than the pulse duration. This is impossible if the femtosecond pulse itself is already the fastest phenomenon available.
However, the wide bandwidth allows for pulse shaping by controlling the spectral phase and amplitude. This allows full control over the temporal shape of the pulse. Spectral shaping can be done in a variety of ways. The spectrum of the pulse can be spatially dispersed by a grating or prism to make the different spectral components spatially accessible. A Spatial Light Modulator (SLM) or deformable mirror (DM) can then impose a certain modulation in amplitude or phase on the dispersed pulse.

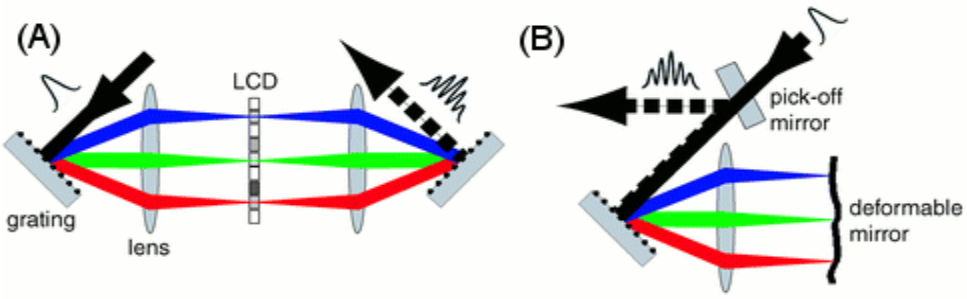

Figure 3.1: Schematic setup of a SLM pulse shaper (a) and a DM pulse shaper (b)[15]

A SLM is based on a LCD screen. It can be either a phase or amplitude SLM. The SLM is placed inside a 4f setup as seen in figure 3.1a. A SLM can have many pixels but the stepwise shaping caused by a finite resolution can cause unintended spectrum modulations[16]. A computer controls the LCD screen inside the SLM to shape the correct pulse. A combination of two shapers can give both phase and amplitude shaping capabilities. This however requires a more complex setup.

Pulse shaping based on a DM has many similarities to pulse shaping with a SLM. A DM is also used in a 4f setup where the spectral components are spatially dispersed as seen in figure 3.1b. A DM consist of a very thin and flexible mirror on top of an array of piezo elements. Each piezo

element can be controlled individually. By applying a voltage to a piezo element it expands and pushes the mirror outwards. This shortens the path length of the light hitting the mirror at that spot. This spectral dependent delay is equivalent to phase shaping.

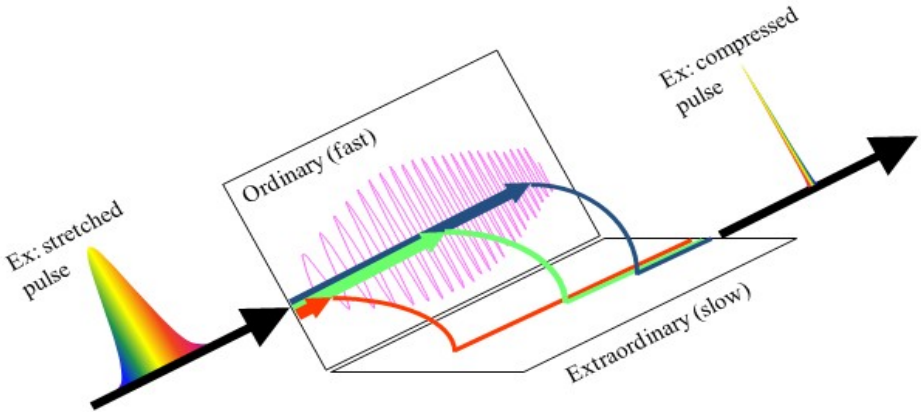

Figure 3.2: Visualization of the interaction between incoming pulse and acoustic wave[17].

An acousto-optic programmable dispersive filter allows full control over spectral phase and amplitude, giving more control over the shape of the pulse. This is achieved by diffraction a pulse with an acoustic wave inside a birefringent crystal from the ordinary polarization to the extraordinary polarization. A visualization of this process is shown in figure 3.2 where a stretched pulse is compressed.

The amplitude of the acoustic wave determines the coupling between the two polarizations and therefore the amplitude of the diffracted wave, while the frequency of the acoustic wave determines which optical frequency is diffracted. By sending an acoustic wave into the crystal with a programmed spectrum, i.e. programmed position and amplitude of acoustic frequencies within the pulse, optical frequencies can be diffracted from ordinary into extraordinary polarization at specific locations within the crystal. As the two polarizations differ in refractive index, the cumulative optical path length (OPL) upon propagation through the crystal will differ as well. The light pulse with extraordinary polarization will have a spectrum with arbitrary modified amplitude and phase, allowing full control over the pulse shape. The transfer function of an AOPDF shaping both the spectral phase $\varphi(\omega)$ and the spectral amplitude $A(\omega)$ is described by:

$$E_{shaped}(\omega) = E(\omega) \cdot A(\omega) e^{i\varphi(\omega)} \qquad 3.1$$

The pulse shaping capabilities of an AOPDF are limited by the finite crystal length, which imposes a limit on the size of the acoustic wave that fits in the crystal. This limits both the dispersion the AOPDF can add to the pulse as well as the spectral resolution.

3.2 Previous work

Pulse shaping (or coherent control) has been applied to many different applications, one of those is high-harmonic generation. A brief overview will be given on the results obtain so far.

The work of Froud et al. show that by varying the second and third order phase of the drive laser pulse the amplitude and wavelength of the harmonics can be influenced[2]. The results show that by

relative simple means of just the second and third order phase the EUV spectrum can already be influenced. The shaping was done using a Dazzler, a similar AOPDF as used in this thesis. The high harmonic generation was done in a 150 μm capillary filled with argon.

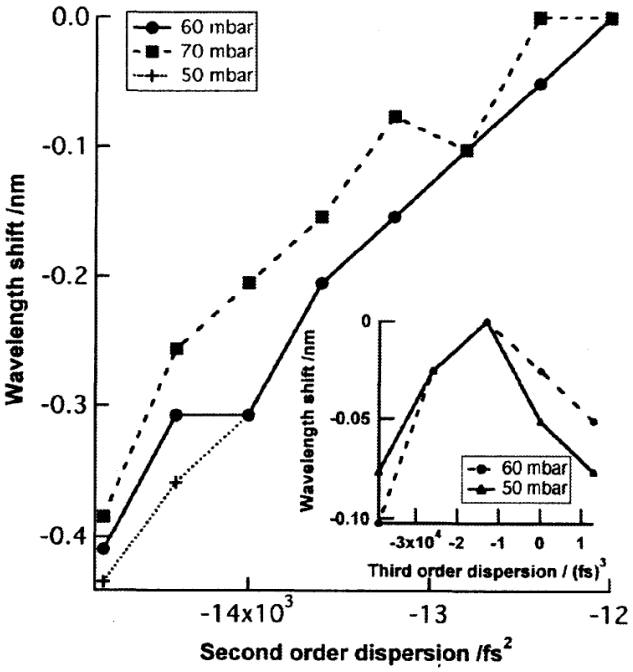

Figure 3.3: Wavelength shift of the harmonics depending on second order and third order (inset) phase[2]

The wavelength shift of the harmonics as function of the second and third order phase at different pressures can be seen in figure 3.3. The wavelength shift found is almost 10% of the adjacent harmonic spacing.

The setup of Froud et al. is similar to the setup used in this thesis and can be used for comparison of the results. Both use an AOPDF as pulse shaping method and use an argon-filled capillary. The notable difference is the capillary diameter and pulse energy. The capillary diameter used in this thesis in 500 μm in diameter compared to 150 μm. The pulse energy used in this work is also higher, about 5 mJ compared to 1 mJ. The differences in setup may explain a difference in the results as well.

A good example in selective enhancement is the result obtained by Bartels et al[3]. The 27th harmonic shows a peak enhancement of a factor 8 and a fourfold increase in contrast between the 27th and adjacent harmonics. The optimization process can be seen in figure 3.4. The enhancement of the 27th harmonic in the spectrum increases with each interaction of the evolutionary algorithm. Some degree of tuning is also found by shifting the spectral window from optimization to the red or blue side of the pulse.

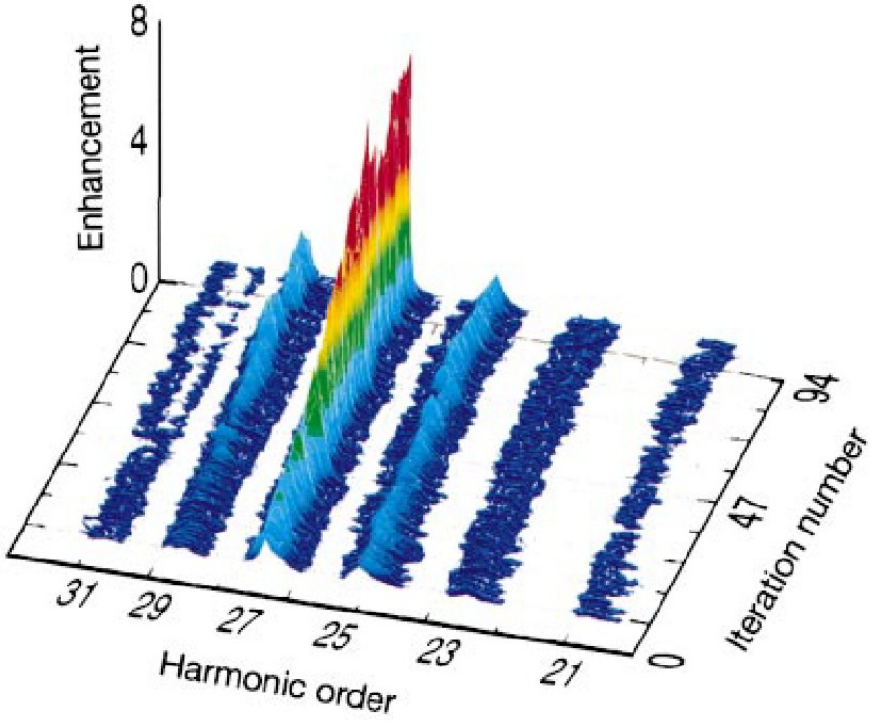

Figure 3.4: Optimization of the intensity of the 27th harmonic relative to the adjacent harmonics.

The shaping is done with a DM controlled by an evolutionary algorithm. Again an argon filled capillary is used, this time with a 175 μm diameter. The laser used has a 80 nm bandwidth and 1 mJ energy. Even though a DM is limited to phase shaping only, the resulting enhancement is significant.

A different approach is given by Reitze et al[4]. Here a 1 mm long argon filled gas cell is used. The shaping is done using an AOPDF in combination with a learning algorithm. The difference in geometry should make interesting comparison. The drive laser used provides 6 mJ pulses with a duration of 30 fs.

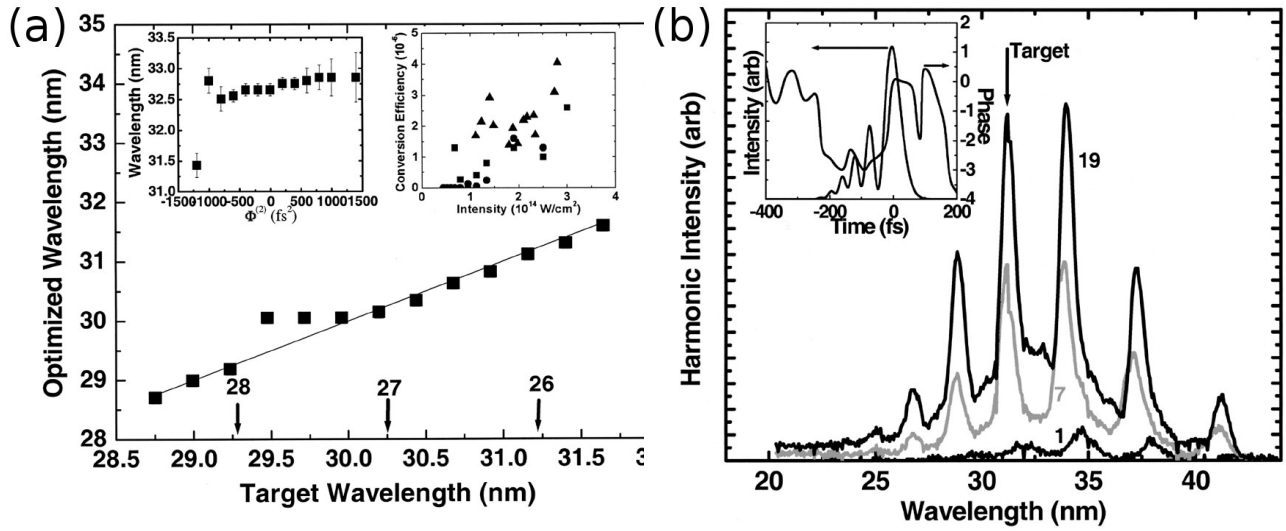

Figure 3.5:Tuning (a) and enhancement (b) obtained by Reitze et al. A 1 mm argon gas cell is used with a 6mJ pulse of 30 fs[4].

The results of the pulse shaping can be found in figure 3.5. The tuning demonstrated nearly covers the gap between adjacent harmonics. Only a small 0.6 nm gap remain for continuous tuning.

3.3 Goal

The goal of the shaping experiments is to have full control over the HHG spectrum. This means arbitrarily enhancing and suppressing harmonics and the capability of tuning the harmonics continuously to close the gap between the harmonics.

Enhancing a single harmonic while suppressing the others effectively creates a monochromatic EUV light source. This can be used for diffractive imaging. The enhancement of a single harmonic regardless of the strength of the other harmonics is useful for seeding a FEL as only the power in a single harmonic is important here. The wavelength tuning of a harmonic will create a tunable seed source.

The shaping is done using an evolutionary algorithm and is discussed in detail in the next section. The fitness function is defined to favor the enhancement of a certain harmonic with the possibility of suppressing others. Tuning is achieved by favoring a wavelength-shifted harmonic.

3.4 Evolutionary algorithm

The evolutionary algorithm (EA) used is a Covariance Matrix Adaptation Evolutionary Strategy (CMA-ES)[18]. The EA is ideal for optimization in a search landscape containing discontinuities, sharp bends or ridges, noise and/or local maximums. This allows the EA to be used on non-smooth, discontinuous and noisy optimization problems where on the other hand optimization strategies such as a hill-climbing algorithm (HC) can easily present a local maximum as the optimum solution.

The EA operates as follows. It samples several new candidate solutions from a multivariate normal distribution which form the individuals in the population. Each individual in the population consists of values for each parameter, also known as the genes. Dependencies between variables of the multivariate distribution are described pairwise in a covariance matrix. Covariance matrix adaptation is a method of updating the covariance matrix of the distribution depending on the fitness of the individuals. The fitness is determined outside of the EA and is a single value representing the successfulness of the optimization for an individual.
There are very few parameters of the EA available to be set by the user of which the population size p_n and the number of individuals with the highest fitness p_f that is used for updating the covariance matrix are the most significant. This makes the algorithm easy in usage and no tedious parameter tuning is needed.

The EA is used in a feedback loop to supply the fitness of the population generated. The parameters of each individual in the population are used as constants for the settings of the Dazzler. The fitness is then determined from either the SHG power or the EUV spectrum depending on the experiment. The fitness is fed back to the EA which produces the next generation.

4
Experimental setup

In this chapter the experimental setup is discussed. First an overview of the setup is given followed by a more detailed description of the different parts. The focus in this chapter is on the design and implementation of the components with the aim of creating an optimal and reliable HHG setup.

4.1 Overview

The complete system consists of a drive laser, focusing optics, the capillary in which the high harmonics are generated, and an EUV diagnostic station for measuring the characteristics of the generated EUV light. The drive laser is equipped with a Dazzler (AOPDF) mounted in between the oscillator and amplifier. To avoid self-phase modulation of the drive laser beam, it is injected into a vacuum system as soon as it leaves the amplifier. A focusing mirror is placed along the optical beam path and places the focus of the drive laser pulse at the entrance of the capillary. An EUV diagnostic station is installed to analyze the emitted harmonics. Several diagnostics are placed along the optical beam path to ensure proper working of the setup and to monitor under which conditions the measurements are taken. The alignment of the complete system is not straightforward and therefore a procedure for aligning the system is given in Appendix A. The system will be described in more detail in the following sections.

4.2 Drive laser

The drive laser is a Coherent Legend Elite Duo USP femtosecond laser system capable of delivering 35-fs 8-mJ pulses at a 1-kHz repetition rate. The high pulse energy and short pulse length of the focused drive laser pulse provide the intensity needed for efficient HHG. The laser uses Chirped Pulse Amplification (CPA) to amplify the seed pulses from the oscillator to a pulse energy of up to 8 mJ. The oscillator pulses are first temporally stretched to lower the peak intensity before being amplified by the regenerative amplifier (RGA). Two Pockels cells control the switching of the pulse in and out of the RGA. After the RGA, a single pass amplifier amplifies the pulse to its final energy before it is temporally compressed to approximately 35 fs.

The oscillator is a Coherent Mantis mode-locked Ti:Sapphire laser capable of delivering the ultrashort pulses needed for HHG. The output is a 80 MHz pulse train with a power of more than 400 mW. The bandwidth is larger than 70 nm and is centered around 800 nm. The Mantis uses chirped mirrors to compensate the dispersion in the laser cavity and is pumped by an optically pumped semiconductor laser. This allows for a very compact laser. The low pulse energy of the Mantis is increased by the amplifier. The oscillator is protected by an optical isolator from unwanted feedback from the amplifier. For shaping of the laser pulse, a Dazzler is installed after the optical isolator and inside the amplifier before the stretcher. More on the Dazzler can be found in section 4.3.

The first step in the CPA process of the amplifier is the stretcher. The stretcher adds a strong positive chirp to the seed pulse, stretching it to several hundred picoseconds. After the stretcher the pulse is sent to the RGA.

The RGA consists of a Ti:Sapphire crystal as gain medium, two Pockels cells to switch the pulses in

and out of the cavity and several cavity mirrors. The cavity is z-folded to conserve space. The Ti:Sapphire crystal is first pumped to obtain maximum inversion. Then one of the Pockels cell is used to inject a single pulse into the RGA. The RGA amplifies the seed pulse of a few nJ for a number of roundtrips until saturation occurs, typically at a few mJ. Then the second Pockels cell is activated to eject the pulse from the cavity. Switching is done by changing the polarization of the optical pulse, such that the pulse is either injected into or ejected from the RGA cavity by polarizers placed in the optical beam path.
Each roundtrip also adds dispersion to the pulse from the optics in the RGA cavity. The stretcher and compressor are adjusted to deliver the shortest output pulse considering all dispersion in the amplifier for a specific number of roundtrips in the RGA and the chirp of the oscillator. This roundtrip time is chosen to be the first roundtrip where the RGA is in saturation. The output power of the RGA in saturation is relatively constant over a large range of the seed pulse energy. To avoid damage of the RGA and subsequent optical elements, the bandwidth of the optical pulse injected into the RGA should be at least 28 nm wide.

After the RGA a Single Pass Amplifier (SPA) provides extra amplification for the pulse, typically by a factor of 3 to 4. As the input pulse is already at high energy a single pass through the gain medium already extracts most of the available gain.

The final stage of the CPA process is the compressor. The compressor adds a strong negative chirp to the pulse that is used to compensate the chirp in the oscillator pulse, and the dispersion introduced by the stretcher and the other optical component in the beam path. In particular, for the RGA, the amount of dispersion added to the optical pulse depends on the number of roundtrips. Typically, the optical pulse is switched out of the RGA at the roundtrip where the pulse saturates. The compressor is adjusted to compensate the total dispersion added to the optical pulse for this particular number of roundtrips in the RGA. Selecting a different number either results in a longer pulse (dispersion not fully compensated) or requires readjustment of the compressor to obtain the shortest pulse.

Note that the gain of a Ti:Sapphire crystal is not flat over the bandwidth. Therefore, the central frequency will be amplified stronger than the wings of the spectrum of the input pulse. This is known as gain narrowing of the bandwidth. To correct for this, an inverse Gaussian spectral filter is applied to the input pulse such that the input energy at the frequency of maximum gain is reduced. This method increases the spectral bandwidth of the optical pulse after amplification and allows compression of the optical pulse down to about 35 fs. It is also essential to have a sufficiently wide bandwidth of the input spectrum in order to avoid optical damage of the various components in the beam path.

Although the oscillator delivers a pulse train of 80 MHz, the amplifier is only capable of producing a pulse train at a repetition rate of 1 kHz. This repetition rate is limited by the Q-switched Nd:YLF pump laser. The Pockels cells of the RGA reduce the pulse repetition rate from the 80 MHz down to 1 kHz. The latter is set by the 1 kHz repetition rate of the Coherent Evolution pump laser. This is a Q-switched and frequency doubled (527 nm) Nd:YLF laser that simultaneously pumps the Ti:Sapphire crystals in the amplifier. The 1 kHz signal of the pump laser provides the master trigger for the amplifier and external devices.

Reliable and stable operation requires that the amplifier is driven into saturation. This requires a sufficient input energy of the optical pulse. At the same time, the spectral bandwidth must be

sufficiently large to avoid optical damage inside the amplifier. By inserting the Dazzler in between the oscillator and amplifier, the energy of the optical pulse transmitted through the Dazzler is reduced by approximately a factor of 4. This requires the Mantis oscillator to also operate stable and reliably. Unfortunately, the Mantis oscillator shows a significant drift that causes the output to drop and increase the risk of losing the mode-locking.

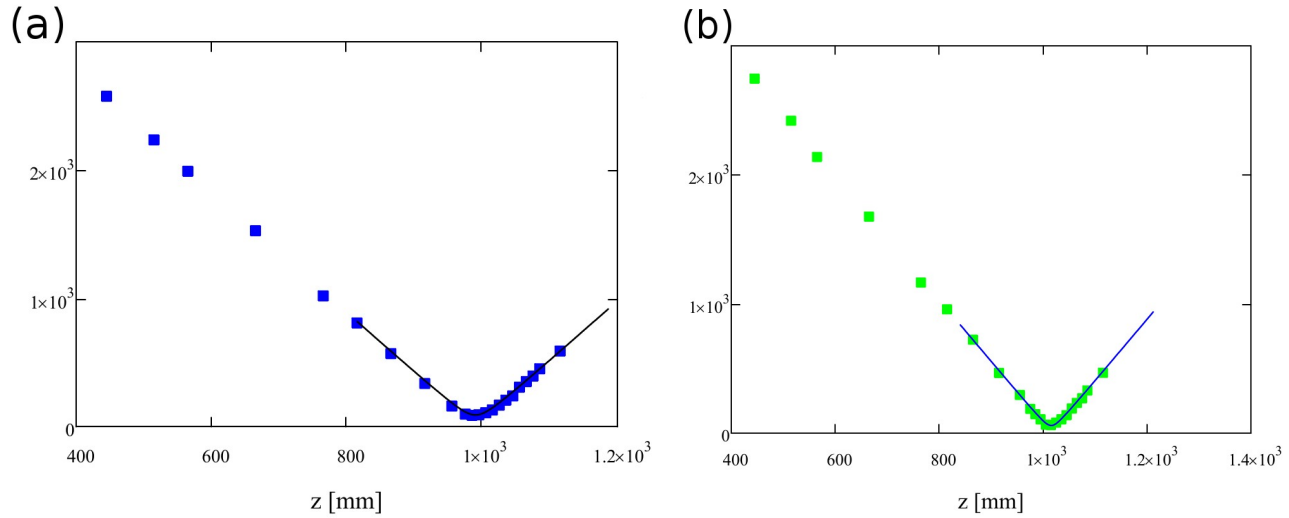

Figure 4.1 : M^2 measurement of the drive laser beam using a 1000 mm lens to focus the beam. (a) Beam waist in x direction, showing a beam waist location of 990mm. (b) beam waist along y direction, showing a beam waist location of 1015mm.

The drive laser beam has astigmatism. An M^2 measurement was done to characterize the beam by measuring the beam cross section at several positions before and after the focal position. The lens used has a focal length of 1000 mm. The results are plotted in figure 4.1 and show that the minimum beam waist is different in size and location for the x (a) and y (b) direction. The beam waist location is 990 mm and 1015 mm for the x and y direction respectively. This astigmatism must be compensated to obtain a flat wavefront in both x and y plane which is needed to couple the drive laser efficiently into the capillary. This is discussed in detail in section 4.4.

4.3 Dazzler

The Dazzler is an AOPDF system made by Fastlite. The Dazzler allows arbitrary spectral phase and amplitude shaping. The system consists of an RF driver controlled by a dedicated computer and a crystal module placed in the oscillator beam. The whole dazzler setup can be seen in figure 4.2. The Dazzler model used is the Dazzler HR 800. The fine resolution of 0.3 nm allows precise and complex shaping. The maximum programmable delay as determined by the crystal length is 8 ps.

Figure 4.2: The complete Dazzler system consisting of the RF driver, the crystal module and a dedicated computer running the Dazzler software.

4.3.1 Dazzler software

The dedicated computer runs the software to control the Dazzler RF driver. The software calculates the acoustic wave that the RF generator will generate from the user supplied spectral amplitude and phase functions. The software also sets the trigger and delay parameters for the RF driver. The software also controls and displays the gain to set the RF power. It further allows remote control enable and can combine various (stored) waveform into a single acoustic signal send to the crystal.

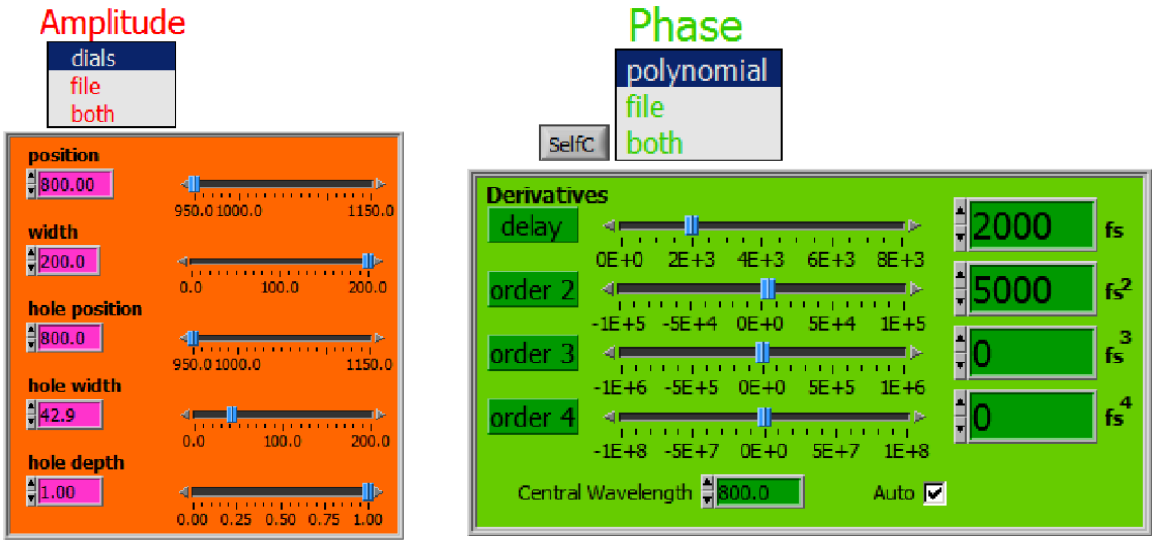

Figure 4.3: Dazzler controls for amplitude (red) and phase (green) shaping.

The spectral amplitude and phase can be set in the software using a series of dials, a user supplied text file or both as seen in figure 4.3. The amplitude function using the dials has limited options. It

allows only a single spectral hole to be set on an otherwise approximately flat amplitude response. The spectral width covered by the dazzler can be set as well as the center wavelength. The hole can be set in position, width and depth. However the user-supplied file option allows a fully arbitrary amplitude shape only limited by the Dazzler resolution and crystal bandwidth. The file is a tab-separated text file listing wavelength and relative amplitude. After an external amplitude profile is read, it is normalized by the software before the whole profile is multiplied by a factor determined by the power settings for the acoustic wave. Furthermore the spectral amplitude is linearly interpolated between given points. The option of the combining the dial settings with the text file is done by multiplying both spectral amplitudes.

The phase shaping capabilities using the dials is restricted to the 1st through 4th order phase. The first order phase introduces only a delay. The delay resulting from the first order phase should be limited to the maximum delay allowed by the crystal length (8 ps). The 2nd through 4th order phase can be used to shape the pulse for experiments or to compensate material dispersion. However, the file option can be used for arbitrary spectral phase shaping. As for the amplitude shaping the text file is a tab-separated file listing the wavelength and phase. The phase between two given points is again linearly interpolated. Combining the dial settings with the text file phase is done by adding the phases. The SelfC button in the control panel sets the phase parameters of the dazzler to compensate the material dispersion of the dazzler crystal, effectively canceling its own dispersion.

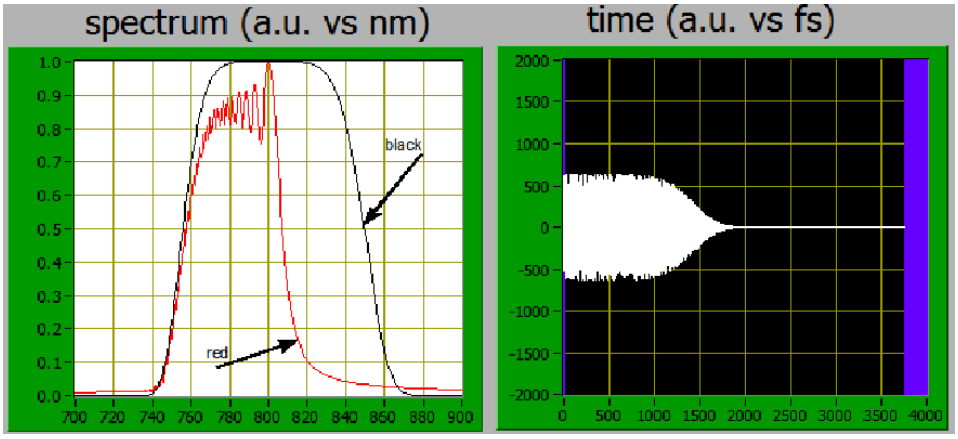

Figure 4.4: The waveform section of the Dazzler software.

In order to inspect the acoustic waveform send to the crystal, the acoustic waveform is displayed on the control panel as seen in figure 4.4, together with the programmed amplitude transfer function (black curve) and calculated transfer function based upon the calculated acoustic wave (red curve). The acoustic waveform is shown on the right and inspection quickly reveals if the acoustic waveform is properly positioned inside the crystal or that clipping occurs. In the case displayed here, the timing of the acoustic wave has not been set properly and the acoustic wave is partly clipped by the limited crystal length. Consequently, the spectrum is clipped as some of the spectral components are not diffracted into the extraordinary polarization by the acoustic wave (due to missing acoustic frequencies). Such a spectrum of the optical pulse transmitted through the Dazzler will be dangerous for the amplifier if the remaining bandwidth is not sufficient to avoid optical damage. This diagnostic section of the control software is therefore very valuable to verify proper operation of the Dazzler.

4.3.2 RF driver

The RF driver is the center of the Dazzler system. The computer, trigger signals and crystal module all connect to the RF driver. It contains a fast arbitrary waveform generator to generate the signal for the piezo driver that generates the acoustic signal in crystal. The nominal power is 10 W into 50 ohm at a frequency of 52.5 MHz. The output is a SMA connector at the front panel and it directly connected to the crystal module using a coaxial cable to reduce electromagnetic interference.

The RF driver has an external trigger input that can be used to synchronize the driver with an external source. In our case, the trigger output of the Coherent amplifier is used to lock the RF driver to the 1 kHz repetition rate of the laser. The delay between the trigger pulse and the optical pulse that is amplified is of the order of 100 ns. Because of the time needed by the acoustic wave to propagate from the generation point to the appropriate volume of the crystal (several tens of microseconds), we set the RF driver to trigger on the previous pulse and set the delay such that the acoustic wave is centered in the crystal when the next trigger arrives. An overview of the optical pulse train in the Ti:Sapphire laser system with Dazzler installed is given in figure 4.5.

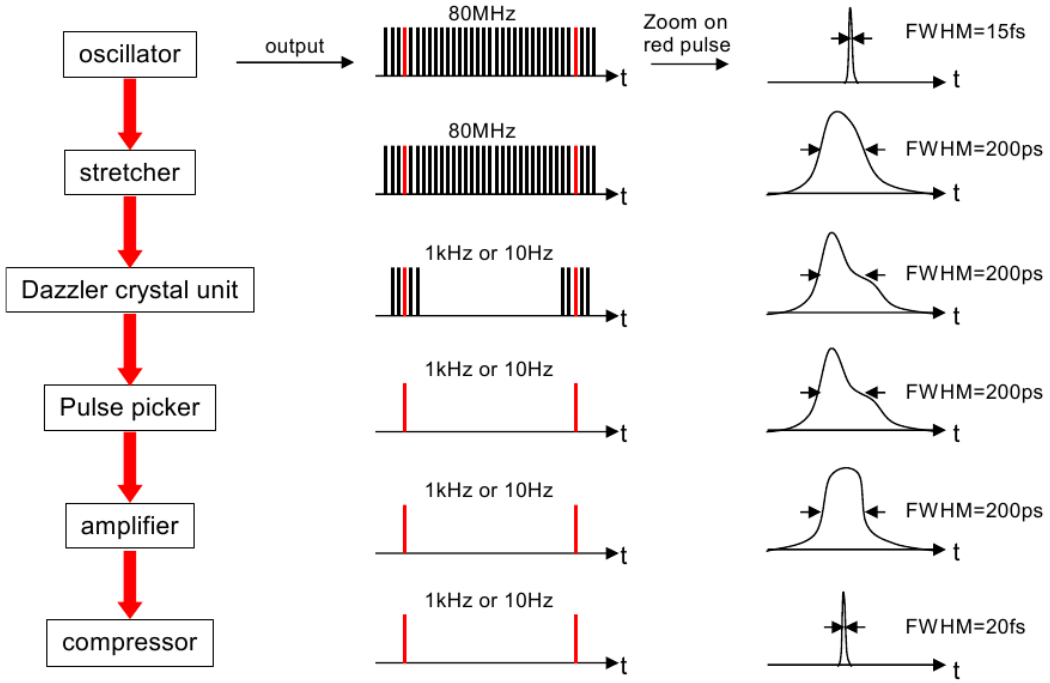

Figure 4.5: Timing diagram of the Ti:Sapphire laser system with Dazzler installed.

4.3.3 Crystal module

The crystal module is the link between the electronics and the optics. A schematic overview of the crystal module and the optical beams can be found in figure 4.6. The injected beam has a polarization along the ordinary axis of the crystal. To match this polarization with the input beam a ½λ waveplate is installed before the crystal module to rotate the polarization of the input beam by 90 degrees. Inside the crystal the beam is only partly diffracted to the extraordinary axis by the acoustic wave as the diffraction efficiency is limited by the maximum amplitude of the acoustic wave that can be generated. After the crystal both the shaped beam of which the polarization is flipped and the undiffracted beam exit the crystal. As the extraordinary axis has a higher refractive index than the ordinary axis the shaped and unshaped beams conveniently exit at an angle with respect to each other.

The crystal module only launches an acoustic wave into the crystal every millisecond to match the repetition rate of the amplifier. This means that the shaped beam consists of short pulse trains with a duration of the acoustic wave inside the crystal. As the average power of the shaped beam is only a fraction of the power of the injected beam the output of the bandwidth detector inside the amplifier is strongly reduced and actually drops below the threshold set for protection of the amplifier. This would shut down the amplifier. Therefore, the bandwidth detector is repositioned to monitor the non-shaped beam as the average power in this beam is hardly changed. The consequence of this it that the bandwidth of the unshaped beam is measured instead of the shaped beam that is used for amplification, and only monitors the bandwidth of the oscillator.

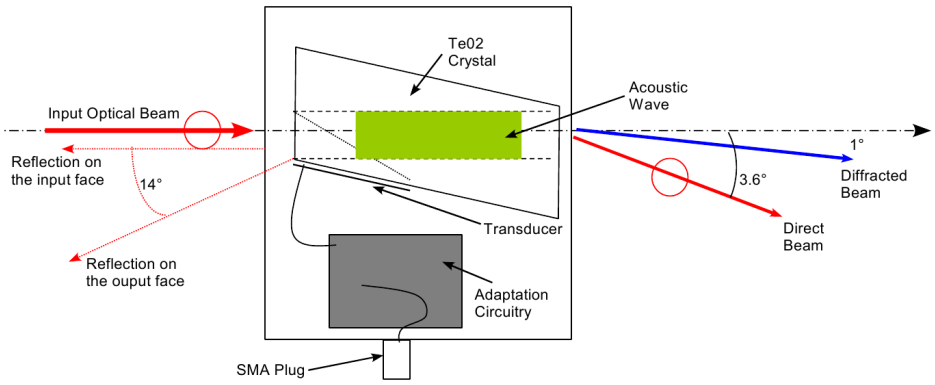

Figure 4.6: Schematic overview of the Dazzler crystal module and the optical beams.

4.4 Focusing optics

The drive laser beam shows astigmatism that causes the focus in x and y direction to be at different locations. To couple efficiently into the capillary the wavefront of the focus must be flat which means that the astigmatism must be compensated. A spherical mirror is used under a non-normal angle of incidence to cancel out the astigmatism. The calculations for the astigmatism compensation can be found in Appendix B.

The optics used are numbered from M1 through M9 for easy reference (see figure 4.7). M1 through M7 are used to steer and focus the beam into the capillary. The retractable mirror M8 and mirror M9 (not shown in figure 4.9) are used for various diagnostic purposes.

Before the laser pulse is injected into the vacuum system, mirrors M1 and M2, which form a periscope rotate the beam by 90 degrees. This flips the horizontal and vertical astigmatism and makes the beam suitable for astigmatism compensation by the spherical focusing mirror while keeping the optical beam in the horizontal plane. The radius of curvature of the spherical mirror (M4) is 5 m, giving a 2.5 m focal length. The matching of the focal spot size to the capillary diameter is discussed in in detail in Appendix B. M4 is placed under a 14 degrees angle to compensate the astigmatism present in the drive laser beam. This angle is calculated using geometrical optics and a detailed description can be found in Appendix B. The calculation were verified by measuring the beam profile along several positions near the focus and agreed with the calculations.

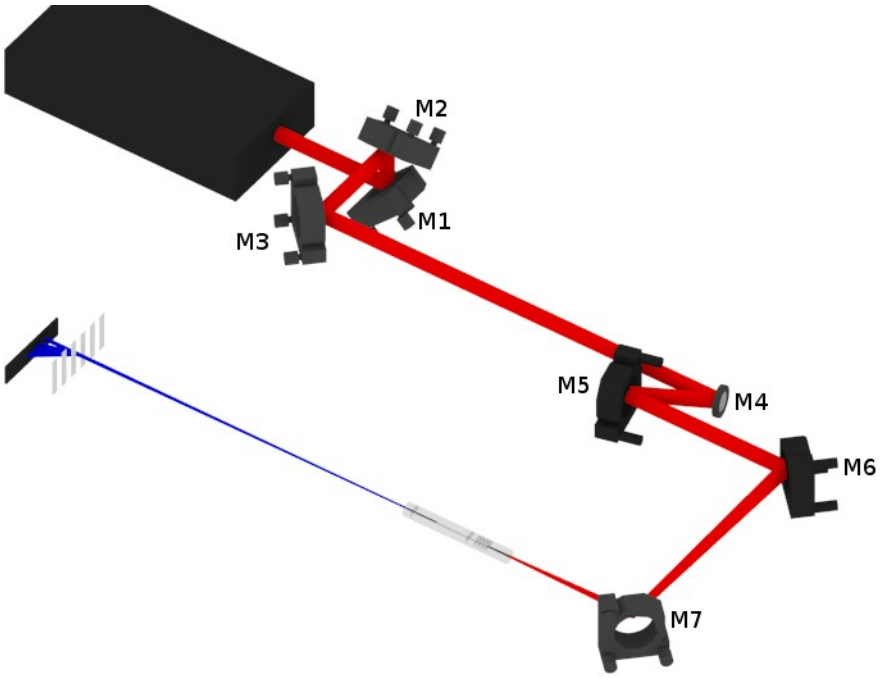

Figure 4.7: Schematic overview of setup consisting of the driver laser, M1 through M7, the capillary and the spectrometer.

The focusing optics are designed to be adjustable when the system is in vacuum. The spherical mirror M4 is fixed in angle to keep the astigmatism compensation constant. M5 and M6 are remotely actuated mirrors and allow full control over both the position and angle of the drive laser at the capillary entrance. The drive laser beam makes a z shape between M4 and M5 which are both mounted on a single linear translation stage. This stage can be used to adjust the distance from the focusing mirror to the capillary entrance within its 50-mm travel range with minimal lateral movement of the focus spot.

The damage threshold of M7 is an important design parameter. Therefore, A CVI TLMB mirror, known for its high damage threshold, is chosen for this mirror. The damage threshold specified for a TLMB mirror is 1.3 J/cm^2 with a 46 fs pulse at 800 nm. When the optical pulse leaves the amplifier it has an energy of 8 mJ with a 12 mm beam diameter (1/e^2). The corresponding peak fluence is 14 mJ/cm^2. After the focusing mirror, the fluence will increase as the diameter of the beam will decrease almost linearly with distance. Placing the folding mirror 50 cm away from the capillary (focal point, f=250 cm), increases the peak intensity by a factor of 25 to a level of 0.35 J/cm^2. This is a factor of 3.7 lower than the damage threshold of the mirror, and the incident fluence should therefore not damage the mirror. Contamination of the mirror surface will lower the damage threshold, so operation in a clean environment is required. If the optical beam contains hotspots, the allowable average fluence may also be lowered to avoid damaging the mirror. To verify that the folding mirror can withstand the incident fluence, the mirror was placed at various positions from the capillary and checked for damage when the laser operated at full power. It was found that the safe minimum distance to the focal point is 85 cm.

4.5 capillary

High harmonics of the drive laser frequency are generated in a glass capillary filled with Argon gas. The function of the capillary is to guide the drive laser pulse and create a long phase-matched interaction length between the drive laser and the harmonics in the EUV.

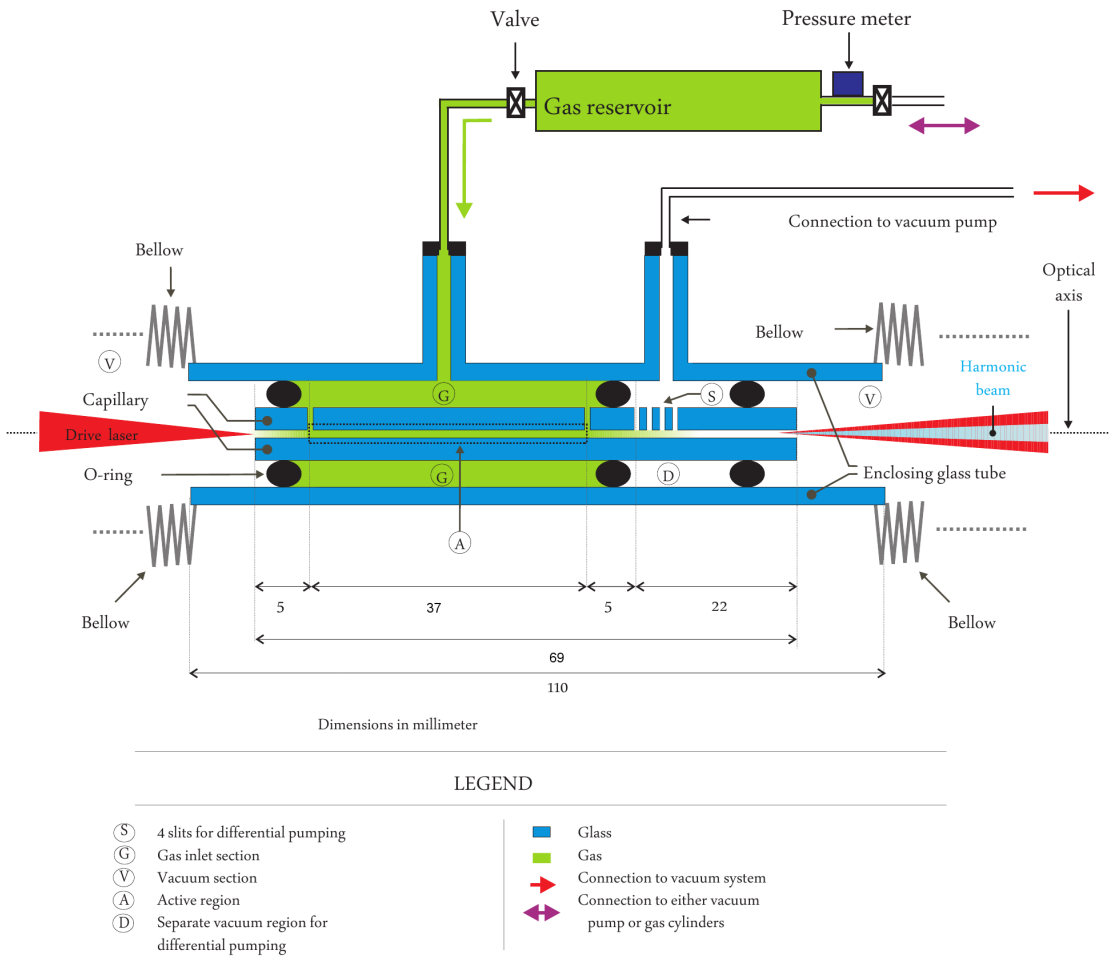

Figure 4.8: Schematic view of the capillary. Adapted from [19].

The capillary used in the experiments has a 37-mm length and a large 500-µm inner diameter. The large inner diameter in combination with the high-energy drive laser pulse should provide a high yield while staying below the critical ionization fraction to allow phase matching. The transmission of the capillary is measured in air and is 87 %, indicating proper guiding of the drive laser beam. This is lower than the 96% incoupling efficiency calculated in appendix B, which can be explained by the imperfect guiding of the capillary and the slits present.

The gas inlet allow the gas to flow into the capillary through two slits (see figure 4.8). To reduce reabsorption of the generated EUV light by the Argon gas, several slits are made in the capillary wall after the interaction region. These slits allow for a differential pumping scheme to quickly reduce the gas pressure in the capillary after the interaction region.

In order to align the capillary with the optical beam of the drive laser, the capillary is mounted on two xy translation stages and connected via bellows to the rest of the vacuum system. This allows careful alignment (4-axis of adjustment) of the capillary.

4.6 EUV diagnostics

To characterize the EUV radiation emitted by the HH source, an EUV diagnostic station was designed and constructed. An overview of the diagnostic station is given in figure 4.9. The core of the diagnostic station is the model DV420 EUV camera manufactured by Andor. If nothing else is inserted in the optical beam path, the camera will measure all the light exiting the capillary. This includes both the IR drive laser pulse as well as the generated harmonics. As the intensity of the drive laser pulse can be larger by 6 orders of magnitude, it needs to be highly attenuated before the EUV radiation can be measured. For this reason a permanent Al filter is placed in the beam line consisting of two 200-nm thick foils. This filter will reflect the IR radiation while the transmission for the EUV radiation is about 60 %. Two foils are used instead of a single thicker foil to avoid leakage of IR light through microscopic holes that are unavoidable in such foils. The filter is placed at a sufficiently large distance behind the capillary (~9 m) to keep the IR intensity below the damage threshold. The diagnostic chamber contains a second retractable filter set, containing, for example, a third Aluminum foil, that can be inserted in the beam line if required. However, this additional filter was not necessary in the measurements taken for this thesis.

With only the IR filter in place, the EUV camera is used to measure the integrated beam profile and total energy of the EUV radiation. When the EUV diagnostic station is run in this mode, the EUV camera can be used to measure the total energy in the EUV radiation, the transverse profile integrated over the pulse duration, the divergence of the EUV radiation (assuming the virtual source is at the exit of the capillary), and the stability of these parameters. Due to the limited aperture of the shutter of 6 mm in diameter, the shutter is placed about halfway between the capillary and EUV diagnostic station (contrary to what is shown in figure 4.9) and is used to block the EUV beam during readout of the CCD. This prevent smearing of the image as the CCD is still sensitive to incoming light during the readout. The shutter is directly controlled from the Andor camera.

To measure the spectrum of the emitted EUV radiation, the diagnostic station also contains a retractable transmission grating and slit (see fig. 4.8). The transmission grating has 3000 lines per mm and the slit has a width of 200 μm. To measure all the diffracted harmonics, the EUV camera is mounted off-center with the use of an adjustable flange. Without the grating (and slit), the displaced camera still captures the complete EUV beam. The camera is used in full vertical binning mode when acquiring spectra. This effectively reduces the camera CCD resolution to a single line. The shutter is not used in this mode.

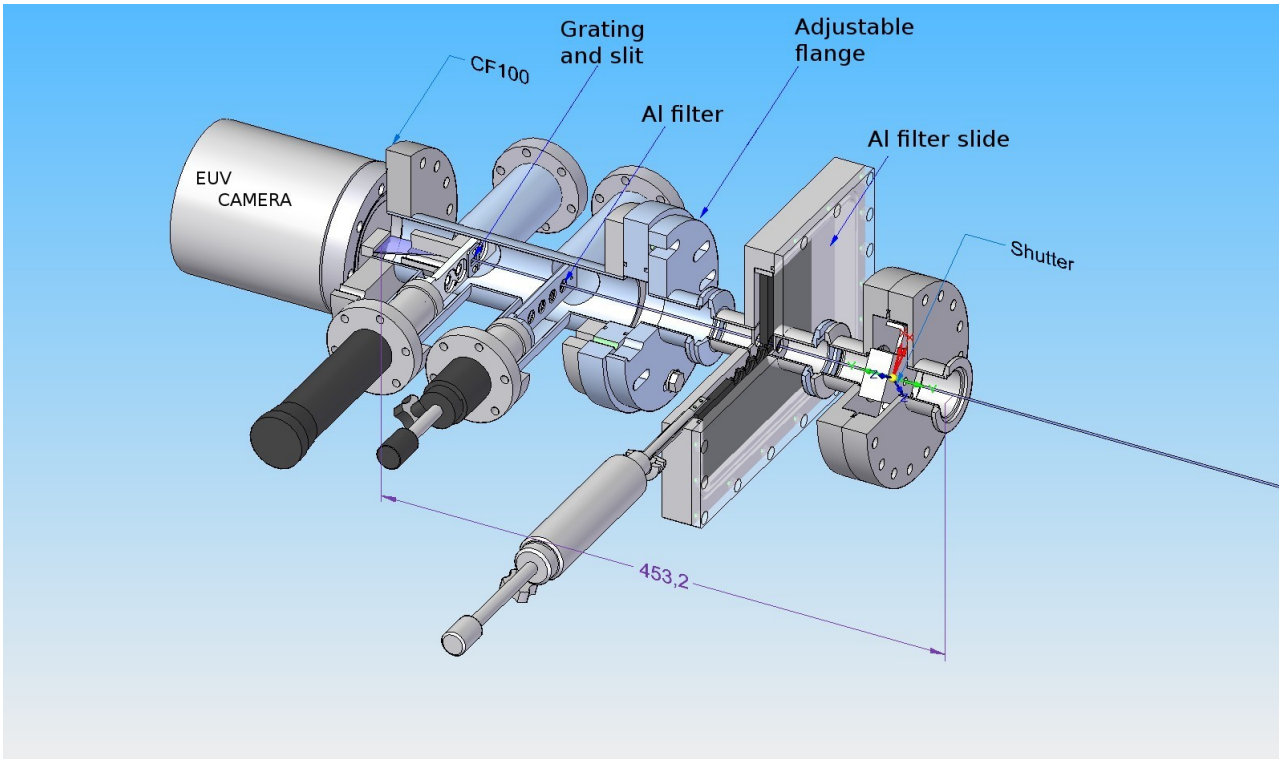

Figure 4.9: A schematic overview of the EUV diagnostic station. Contrary to what is shown here, the shutter is placed in the middle of the beamline.

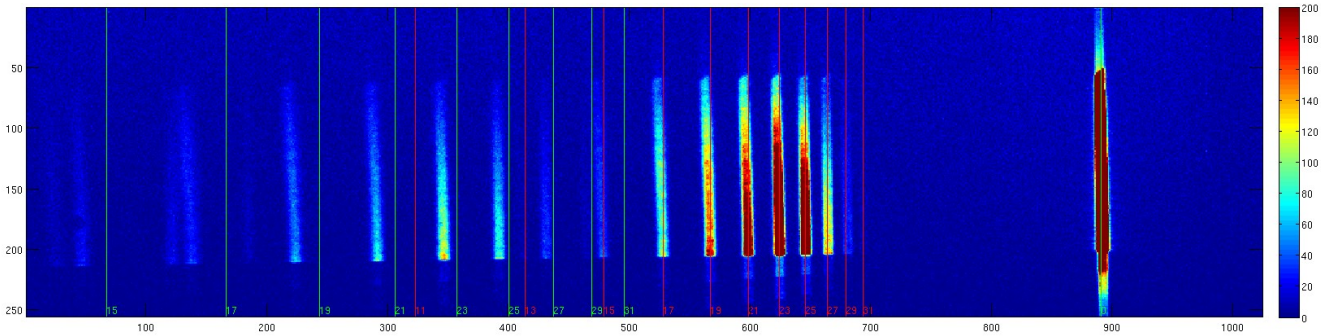

Figure 4.10: A typical high harmonic spectrum as measured by the EUV camera with a transmission grating having 3000 lines per mm and a 200-µm width slit. The calculated location of the harmonics are indicated by the vertical lines, red for the first order diffraction, yellow for the second order diffraction.

The calculated position of the harmonics is obtained by varying the distance from the grating to the camera until a good overlap is obtained between the measured spectrum and the calculated harmonic orders. For the case of fig. 4.10 the calculated distance is 66.5 mm, which is in good agreement with the design value.
The camera used is the model DV420 CCD camera manufactured by Andor. It has a resolution of 1024x255 pixels with a 26 um pixel size. It's large CCD area of approximately 6.6x27 mm is sufficient to capture the beam-profile of the EUV beam. When acquiring spectra the full vertical binning mode of the camera is used. This performs a vertical sum of the pixels by adding their charge during the readout. This allows fast and low noise acquisition of the spectra.
The CCD sensor can also be cooled to reduce noise, however the camera was used at room temperature for the measurements reported in this thesis.

4.7 vacuum system

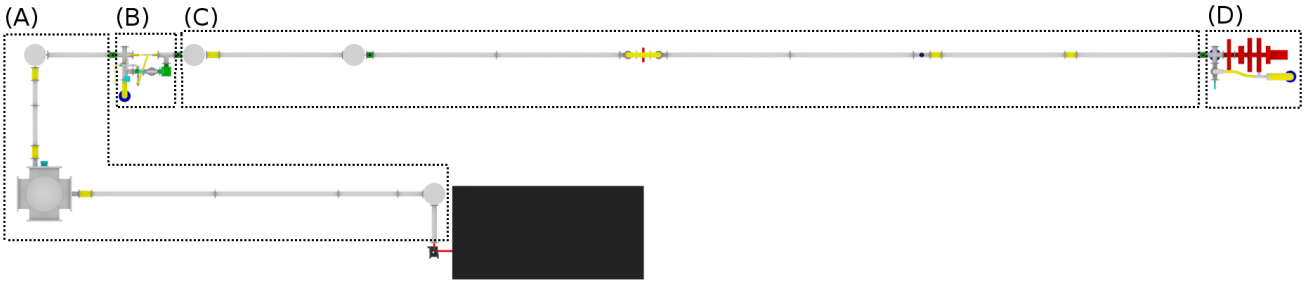

Figure 4.11: Overview of the vacuum system divided in 4 parts.

As mentioned previously, the compressed laser pulse delivered by the laser system has a sufficiently high intensity that it is prone to nonlinear optical effects, in particular self-phase modulation[20]. Therefore, the laser pulse enters a vacuum system immediately after it exits the laser system. The vacuum system extends all the way to the EUV diagnostic station at the end of the optical beam line as the generated harmonics are quickly absorbed in air.

The vacuum system is divided in four sections as shown in figure 4.11. The first section contains the beam transport and focusing optics up to the capillary. The following section contains the capillary and gas pressure regulation. Next is the beamline transport to the EUV diagnostic station, followed by the EUV diagnostic station itself. All sections are separated by valves to allow separate venting and pumping of the sections should any maintenance or realignment be needed. When the setup is not in use the valves are closed to avoid uncontrolled pressurizing of the vacuum system when one or more of the pumps shuts down.

Several bellows are used at strategic places in the system to allow fine adjustment of some of the components in the system and to connect various sections build using fixed length vacuum tubes. However bellows tend to contract when the system is pumped down. To counter this contraction a pair of adjustable rods was manufactured for each bellow. The rods are placed alongside of the bellows to keep their length fixed when the system is pumped down and keep the total length constant.

4.7.1 Transportation and focusing section

The drive laser pulse enters the vacuum system through a 3 mm thick MgF window. The window was optimized to withstand the pressure difference and at the same time minimize its contribution to self-phase modulation of the laser beam. For example, the lower index of refraction of MgF results in a lower contribution to self-phase modulation than that for a Sapphire window, even when allowing for the smaller thickness that a Sapphire window can take.

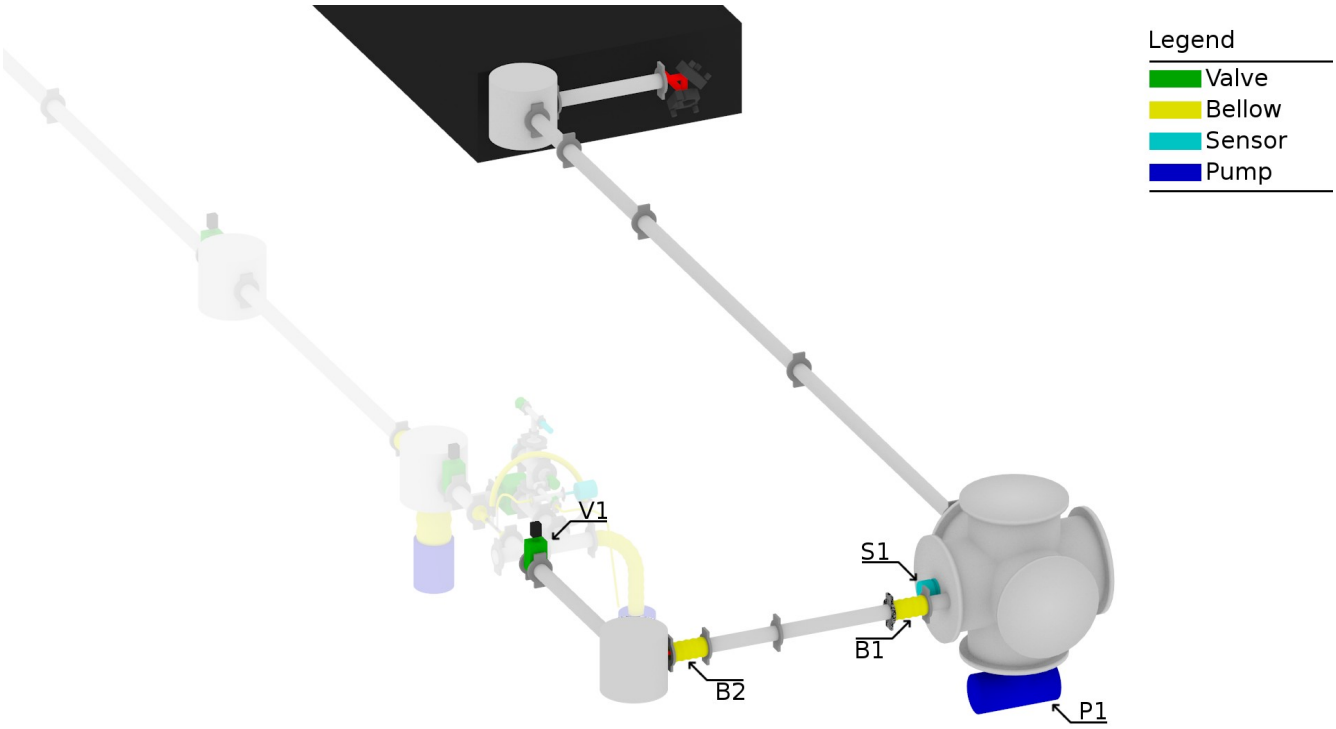

Figure 4.12: The transportation and focusing section of the vacuum system

The first section of the vacuum system holds mirrors M3 through M7 and is shown in figure 4.12. The vacuum system makes a U-turn to transport the beam to the capillary entrance. As the beampath is not linear the small contractions and expansions that occur when the system is pumped down or vented also affect the alignment significantly.

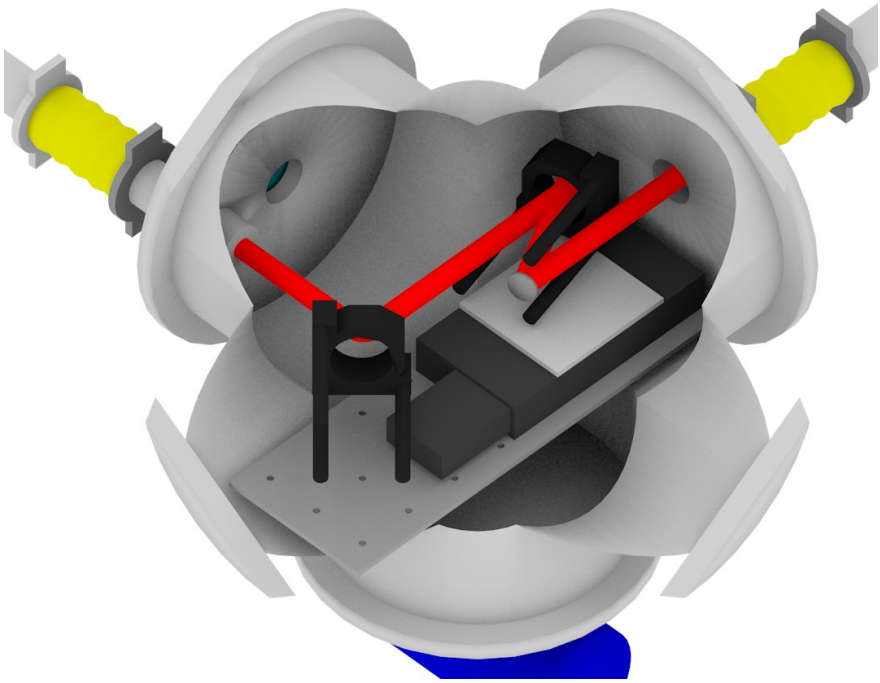

Figure 4.13: Cutaway view of optics inside the 6-way vacuum vessel.

The large vacuum vessel in this part of the vacuum system holds mirrors M4 through M6 as seen in figure 4.13. A small breadboard is mounted inside the vacuum vessel for mounting of the components. The focusing mirror M4 and folding mirror M5 are mounted on a vacuum compatible linear translation stage using a custom mounting plate. M5 and M6 are fitted with a pair of vacuum compatible actuators for movement in both axes. The vacuum vessel has electrical feed-throughs for the actuators and stage as well as a full range pressure sensor (S1 in figure 4.12). The turbomolecular pump of the system is on the bottom of the vessel and a window is on top to check the coarse alignment of the optics. M7 is placed in a small vacuum vessel to steer the beam towards the capillary. This small vacuum vessel has a window to pass the transmission of the folding mirror to M9 (in air, not shown) for diagnostic purposes .

4.7.2 Capillary section

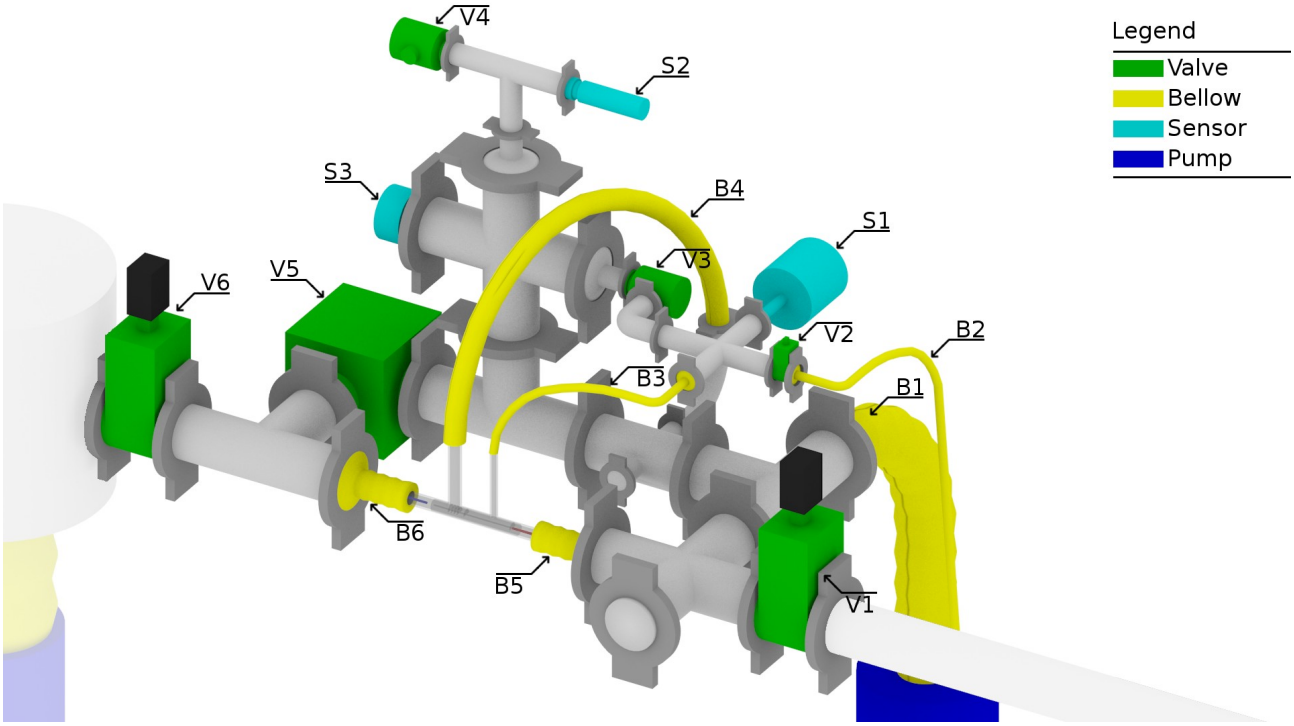

Figure 4.14: The capillary section of the vacuum system. V1 corresponds to V1 of figure 4.12.

The second part of the vacuum vessel is built in a U-shape around the capillary and is shown in figure 4.14. Bellows at both ends of the capillary (B5, B6) connect it to the vacuum system. The capillary is also connected with two hoses, one from the pressure regulator section to the capillary gas inlet (B3) and one from the vacuum system to the capillary outlet (B4). Refer to figure 4.7 for details about the capillary. A Pirani (S2) and cold cathode gauge (S3) pressure meter are connected to monitor the pressure of this part of the vacuum system. This is particularly important when gas is flowing through the capillary into the vacuum system and the pressure rises. A higher pressure is a higher load for the turbomolecular pump of this section. A safe capillary pressure range is 0 to 20 mbar, as this keeps the vacuum system's pressure below $2 \cdot 10^2$ mbar. Capillary pressures up to 60 mbar are possible for short periods of time but should be avoided as the turbomolecular pump runs hot quickly because of the high pressure in the vacuum system. The volume behind the capillary exit can be separated from rest of this section of the vacuum system by closing valve V5. This prevents the increased pressure caused by the gas flow out of B4 into the vacuum system from reaching the capillary exit and beamline section. Pump P1 of the beamline section keeps the volume behind the capillary exit at low pressure.

In order to obtain a constant pressure in the capillary a pressure regulation system is needed. The gas supply is connected to B2 and enters the pressure regulation section via an electronically controlled valve (V2). The pressure regulation section is separated from the vacuum system by valve V3. A highly accurate barometer (S1) is used to measure the pressure inside the regulation section. A pressure controller regulates the pressure by reading the pressure from the analog output of the barometer (S1) and controlling the voltage on the electronic valve (V2). A computer connected to the pressure regulator allows the control and monitoring of the pressure regulator and can set the PID values for the regulation.

4.7.3 Beamline section

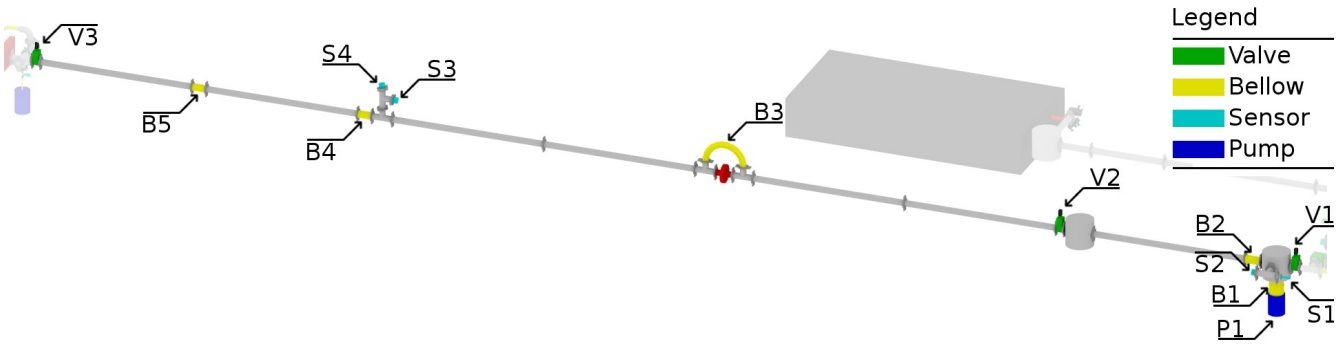

Figure 4.15: The beamline section of the vacuum system. V1 corresponds to V6 of figure 4.14.

The third part of the vacuum system is the beamline from the capillary section to the EUV diagnostics section and is shown in figure 4.15. The vacuum system has two small vacuum vessels and a shutter. The vacuum pump is placed beneath the first vacuum vessel as close to the capillary exit as possible. This is done to optimize the pumping speed in order to have the lowest pressure possible in the beamline. The second vacuum vessel is placed approximately 2 meters away from the capillary to avoid exceeding the damage threshold of the various diagnostics optics. A vacuum compatible shutter is placed approximately 4 meters away from the capillary, the position being determined by the limited diameter of the shutter opening of only 6 mm. To maintain a good pumping speed a bellow (B3) is placed as a bypass. The shutter is not light tight across the full 40 mm vacuum tube diameter. A special aperture was placed before the shutter and the bellow bypass to act as a stray light filter. The shutter is connected to the shutter driver, which is controlled by the camera in the spectrometer. More information on the shutter can be found in the spectrometer section.

A background of argon will reabsorb the generated high harmonics. To keep the reabsorption of the harmonics to a minimum, a maximum pressure of 10^{-4} mbar is set as design parameter for the vacuum downstream of the capillary. The pressure in the section is monitored using two sets of Pirani and cold-cathode gauge pressure meters (S1 through S4). After pumping for a few days a pressure of around 10^{-6} mbar is measured is by S2 and $3 \cdot 10^{-5}$ mbar at S3. The pressure at S2 only increases to $2 \cdot 10^{-5}$ at a 20 mbar capillary pressure.

4.7.4 EUV diagnostics section

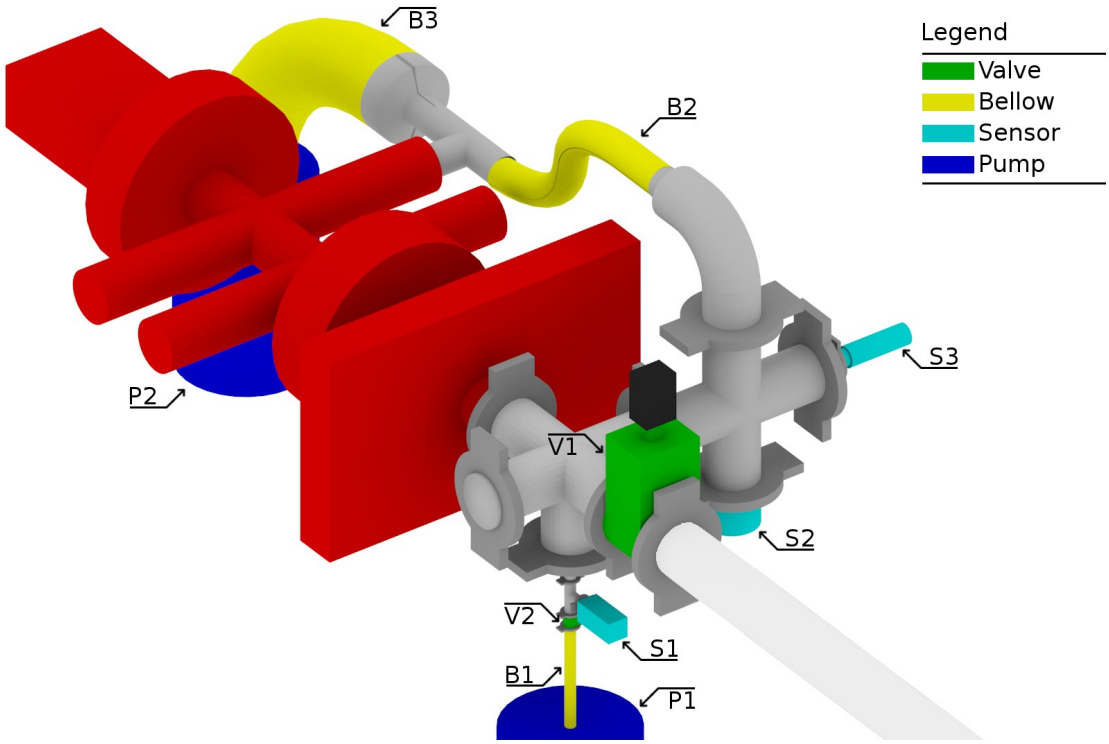

Figure 4.16: The EUV diagnostics section of the vacuum system. V1 corresponds to V3 of figure 4.15. See figure 4.9 for details of the components of the EUV diagnostic station.

The EUV diagnostics section is placed after the beamline section and is shown in figure 4.16.
The EUV diagnostics system is indicated in red and a detailed view of its subcomponents is shown in figure 4.9. One critical component is the Al filter that blocks the IR and transmits the EUV light, and that consists of two 200-nm thick foils. Because of the thin foils used, the pressure should be kept equal on either side of the filter, also when pumping down the vacuum system. Therefore, the filter housing contains a bypass to keep the pressure on either side of the filter equal. This bypass is specifically designed to avoid transmission of any scattered IR light. A slow pumping system is installed to allow the section to be pumped down to several millibar over a period of 30 minutes. This keeps pressure differences inside the EUV diagnostics station to a minimum.
The slow pumping is done with a separate pump (P1), which is limited in pumping speed by a needle valve (V2). The pressure is monitored by a thin film pressure transducer (S1) to accurately monitor the change in pressure.
The camera needs to be kept in a clean environment as contamination of the CCD will lead to increased absorption of the EUV radiation and therefore to a larger uncertainty in the measurement. The EUV light can crack any hydrocarbons present and cause a carbon deposition on optical surfaces[21] such as the filters and the CCD chip. To obtain a low pressure the vacuum pump (P2) is connected to the spectrometer with a short large diameter bellow (B3). The rest of the vacuum system is connected via another bellow (B2). The pressure measured by S2 is $1.7 \cdot 10^{-5}$ mbar.

4.8 Diagnostics

Several diagnostics have been included in the setup for both the drive laser as well as the EUV light. The diagnostics are used to record under which conditions the measurements are taken and to aid in (re)aligning the setup.

4.8.1 Shaped oscillator pulses

To have access to the shaped oscillator pulses, two flip mirrors and 3 fixed mirrors are placed inside the amplifier to route the shaped beam out of the amplifier. This beam is not only used for characterizing the shaped pulse but can also be used for shaping experiments that do not require the full energy that is delivered by the amplifier. As the oscillator delivers a continuous train of femtosecond pulses at a repetition rate of 80 MHz, the shaped beam also contains a train of pulses for the duration that the acoustic wave is present in the crystal. Note that the leading and trailing pulses of this train will not be properly shaped as the acoustic wave only partly fills the crystal. A pulse picker is required to filter out the properly shaped optical pulses. Still, as the improperly shaped pulses only take up a small fraction of the pulses in the shaped beam, the average response to the shaped pulses still can provide useful information. The shaped pulse spectrum is the spectrum of the pulse that would enter the RGA. The spectrum of the shaped pulses depends on both the oscillator spectrum and the Dazzler spectral shaping settings (amplitude and phase).

4.8.2 Focal spot monitoring

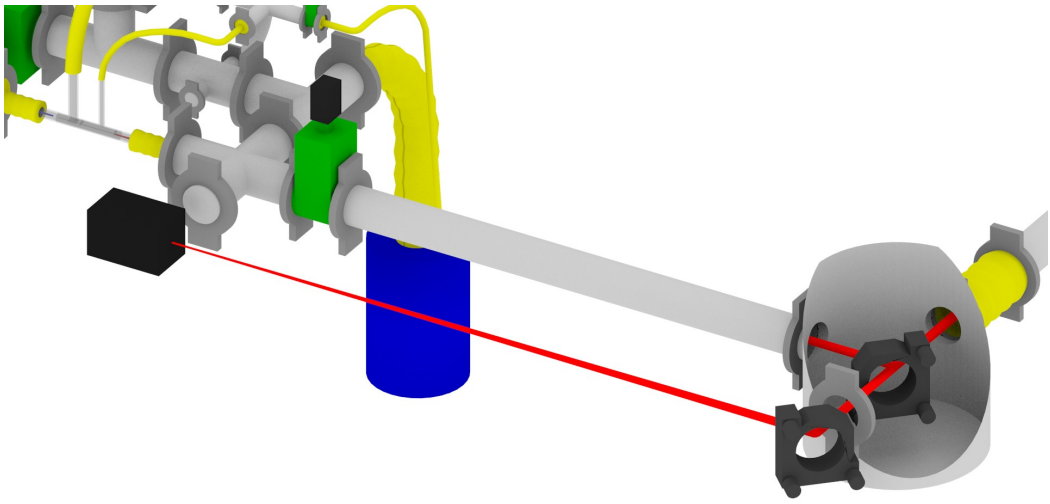

Figure 4.17: Schematic view of the transmitted beam of M7 passed to a camera via M9.

In order to measure the characterize the optical beam at the entrance of the capillary, we place a camera at an appropriate distance behind mirror M7 to create an equivalent position of the capillary entrance as seen in figure 4.17. The transmission of a TLMB mirror (M7) is very low, but as the beam is focused on the camera the intensity is high enough for the camera to give a reasonable signal. A folding mirror (M9) is used as the space available is limited. This allows to monitor the beam profile at the focal position, i.e., entrance of the capillary and also allows for a coarse alignment of the drive laser to the capillary if alignment is lost; provided that M7 and M9 remain stable with respect to the capillary. Accurate alignment of the laser to the capillary was done using other methods such as monitoring the drive laser beam after the capillary or minimizing the plasma generation of the drive laser at high power.

4.8.3 Beamsplitter

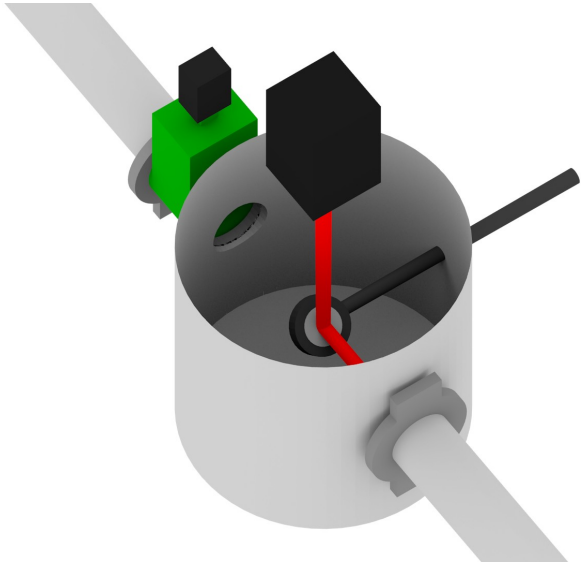

Figure 4.18: Schematic view of M8 reflecting the transmitted drive laser beam to a camera

Monitoring the drive laser beam exiting the capillary during alignment provides a check to see if the drive laser is coupled properly into the capillary. A 10% beamsplitter is placed about 2 meter away from the capillary exit to reflect the drive laser beam to a camera as shown in figure 4.18. The beamsplitter can be moved in and out of the beam path to either pass the EUV to the spectrometer or to reflect the drive laser beam to the camera placed above the vacuum system. A beamsplitter was chosen to lower the thermal stress on the neutral density filters placed in front of the camera. The beamsplitter is fluorescent under the EUV light and is therefore used as a diagnostic to check if any high harmonics are generated.

4.9 Second harmonic generation

In order to test the pulse shaping and the evolutionary algorithm, the shaped oscillator pulse is ejected from the amplifier and focused on a BBO crystal for second harmonic generation (SHG). The evolutionary algorithm is set to optimize for maximum second harmonic signal as this would lead to the shortest pump pulse.

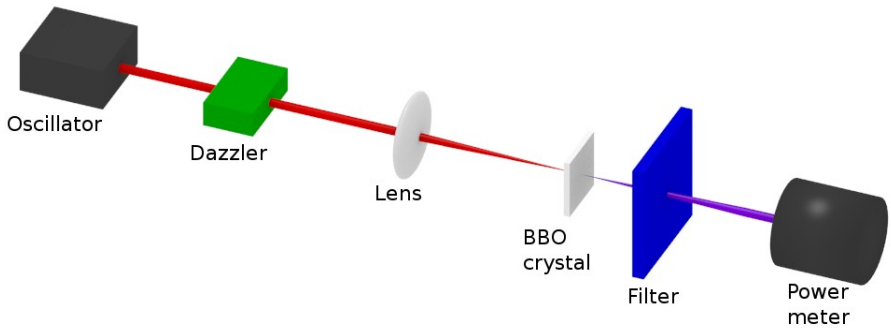

Figure 4.19: Schematic overview of the SHG setup

A schematic overview of the SHG setup is given in figure 4.19. The shaped beam is focused by a focusing lens with a 10-cm focal length. A 100-μm BBO crystal is placed in the focal point for maximum intensity. A 3-mm Schott BG-40 colored glass filter is placed after the BBO crystal to filter out the shaped beam and pass only the generated second harmonic which is then measured by an HP optical power meter. The detector used was calibrated only in the 450-1020 nm interval. The 450-nm setting is used for all measurements. This slightly underestimates the actual power of the SHG signal but as only relative power is important for optimizing the pulse shape this was not compensated. The HP optical power meter is remotely read out by the computer running the EA. The measured SHG power is used as the fitness for the trial pulses generated by the EA.

5
Measurement results

In this chapter the measurements performed with the HHG setup are presented. We start with the characterization of the EUV beam followed by testing and characterization of the evolutionary algorithm. Then we present the pulse shaping measurements using second harmonic generation (SHG) and finally we present the results of the pulse shaping for high harmonics generation.

5.1 HHG beam analysis

A series of beam-profile and spectrum measurements of the EUV beam are done to characterize the HHG setup. The beam pointing needs to be stable from shot to shot, not only to keep the beam reliably on the spectrometer, but a stable pointing is also important for applications like seeding of free-electron lasers. Furthermore, the evolutionary algorithm is expected to function better with a stable and reproducible EUV output. Fluctuations in total EUV energy and/or spectrum may have an adverse effect on the decisions made by the evolutionary algorithm that are based on these parameters.

A good understanding of the behavior of the EUV beam under various conditions is thus necessary to understand the behavior and results of the evolutionary algorithm.

5.1.1 Beam pointing stability

The EUV beam-profile is measured at different gas pressures. The beam position was not stable in time, as illustrated in figure 5.1, which shows a series of captured beam-profiles measured at 0.3 s interval with a 20 ms integration time for a drive pulse energy of 7.5 mJ and a pressure of 12 mbar, and in figure 5.2, which shows the x- and y- coordinate of the center of mass of the EUV pulse for a series of subsequent measurements.

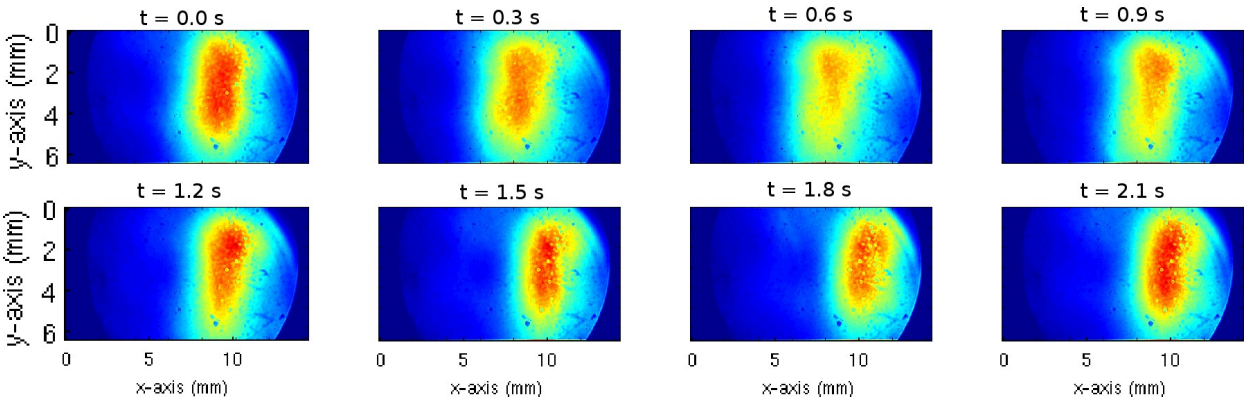

Figure 5.1: Sequentially captured beam-profiles. A clear horizontal oscillation is visible.

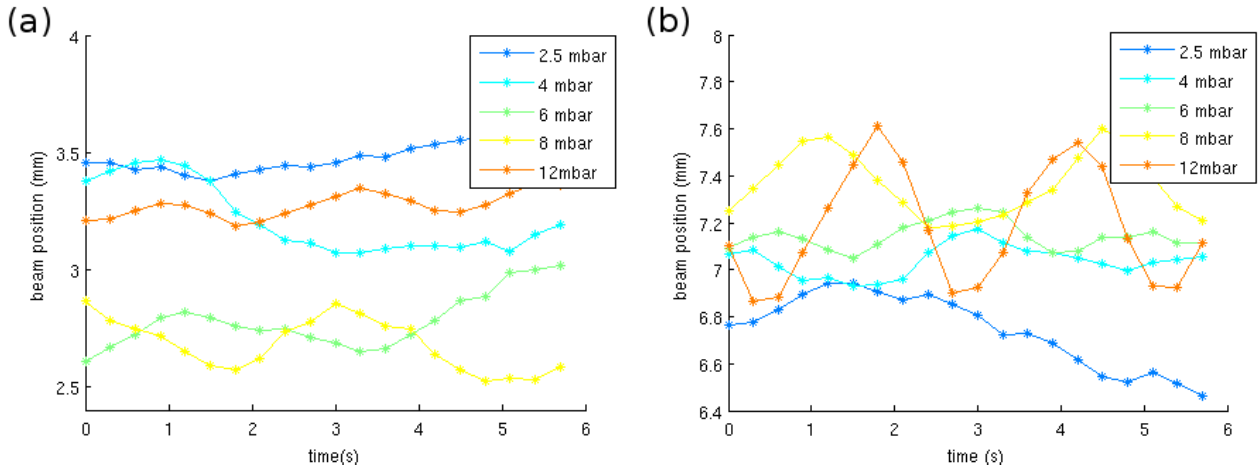

Figure 5.2: X (a) and y (b) position of the center of mass of the EUV pulse for subsequent measurements at a rate of 3 Hz.

Figure 5.2 clearly shows that the motion of the center of mass is more pronounced in the x-direction than in the y-direction and that the frequency and amplitude of the oscillations in the x direction increases with pressure. At a pressure of 12 mbar, the oscillation period is approximately 2.5 s. We were not able to identify a source that can produce a frequency of around 0.4 Hz, and that may be pressure dependent. The variation in beam pointing will affect the spectrum measurement, as a single slit is mounted in front of the transmission grating. The motion of the EUV beam affects which part is transmitted through the slit and illuminates the grating and hence affects the stability of the resulting spectrum.

5.1.2 Beam size vs pressure

We also have investigated the size of the EUV beam at the location of the camera as a function of the pressure inside the capillary. Again, the drive laser pulse energy is 7.5 mJ and the integration time 20 ms. Figure 5.3 shows typical beam profiles for pressures ranging from 1.7 to 12 mbar. The beam profile is nearly round for pressures between 2.5 and 4 mbar.

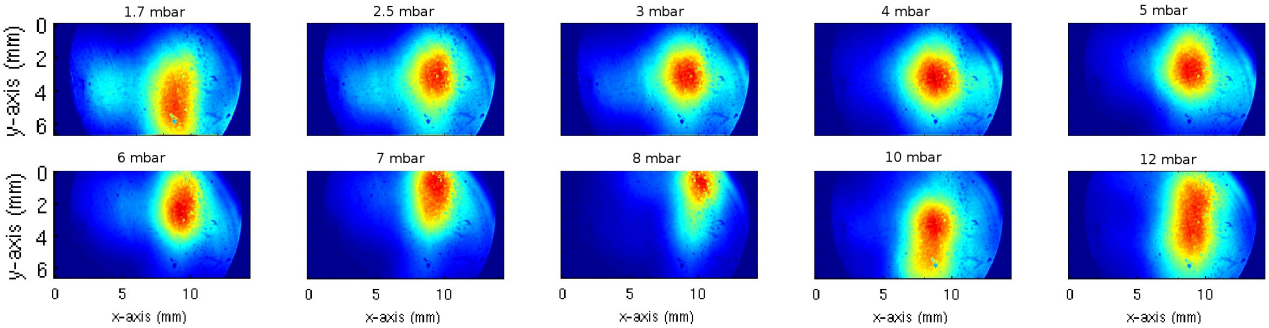

Figure 5.3: Typical beam profiles pressures ranging from 1.7 to 12 mbar at 7.5 mJ

The rms width in both the x- and y-direction is calculated from these profiles and can be found in figure 5.4. An average value is calculated by averaging over 20 single measurements with each measurement integrating 20 pulses.

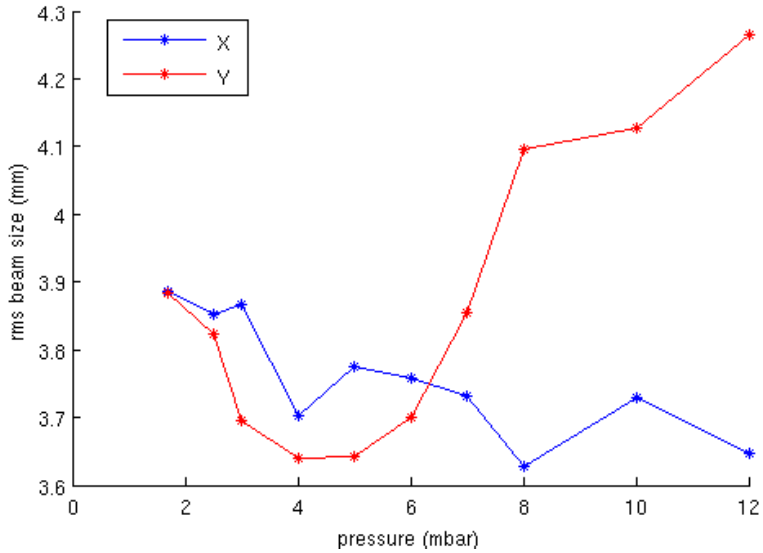

Figure 5.4: Rms beam size calculated for pressures from 1.7 mbar to 12 mbar for x and y direction.

The calculated beam size shrinks in the x-direction with increasing pressure and the y-direction beam size shows a minimum around 4 mbar. The calculations show that the beam is asymmetrical at pressures above 6 mbar with the beam size in the y-direction being larger than the x direction. The EUV beam is nearly round for a pressure of 5 mbar, which corresponds to the phase-matching pressure for most of the harmonics (see figure 5.6).

5.1.3 Spectral stability

The stability of the spectrum is investigated for pressures ranging from 1.7 mbar to 12 mbar by taking 20 measurements with a 0.3 second interval. The integration time used for each measurement is 20 ms.

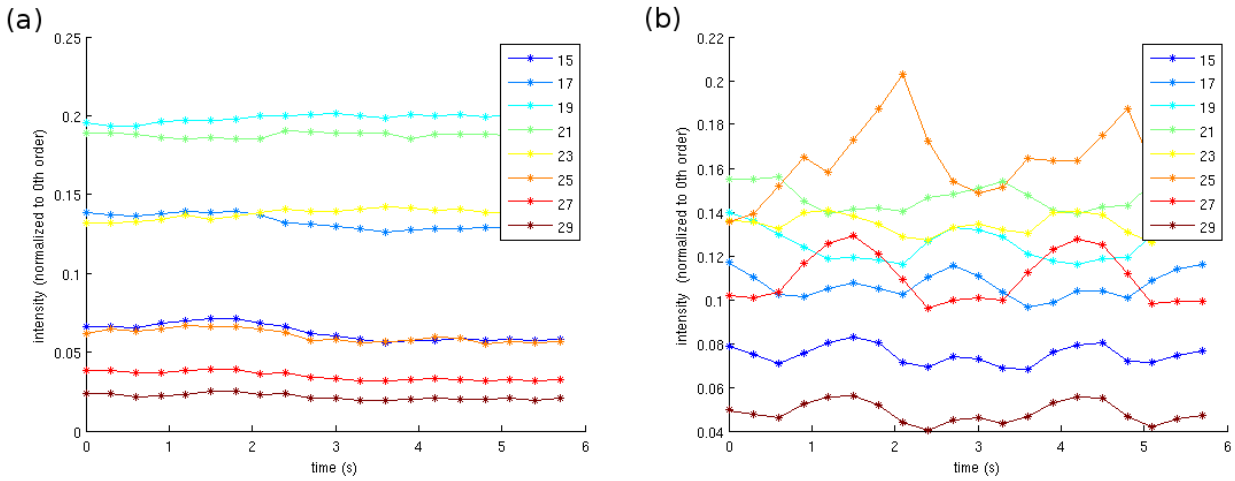

Figure 5.5 : Intensity of each harmonic (normalized to the 0th order peak) for subsequent measurements at a rate of 3 Hz for a pressure of 3 mbar (a) and 10 mbar (b). The drive laser pulse energy is 7.5 mJ.

The intensity of each harmonic is calculated from the CCD image by summing the counts in the area corresponding to a particular harmonic, as seen in figure 4.10. The total count of the harmonic is normalized with the counts of 0^{th} diffraction order which is proportional to the intensity of the

EUV beam. By normalizing the spectra, it should not be sensitive to the pointing instability of the EUV beam. At 3 mbar the intensity is approximately constant in time but at 10 mbar there are oscillations visible in the intensity of several harmonics. From figures 5.2 we know that the center of mass of the EUV beam is approximately constant for a pressure of 3 mbar, and the slit therefore samples the same part of the EUV pulse. For a pressure of 10 mbar, the variation in the center of mass in the y-direction is limited to about the width of the slit, while in the x-direction the variation is much larger. Since the slit is along the y-direction, the variation of the center of mass in the y-direction will not change the position in the EUV pulse where the spectrum is measured, while for the much larger variation in the x-direction this means that the spectrum is measured for different parts of the EUV pulse. As the observed oscillation frequency in the relative intensity for a pressure of 10 mbar is approximately the same as the oscillation frequency observed in the center of mass, this may indicate that the relative spectrum is not constant over the cross section of the EUV pulse.

5.1.4 Pressure dependence of high-harmonic generation

The efficiency of high-harmonic generation in a capillary can be increased through pressure phase matching as shown in chapter 2.2. By correctly setting the pressure, the phase mismatched that is introduced by the dispersion due to the free-electron density and the geometry of the capillary can be compensated by the dispersion due to atoms in the capillary. By changing the pressure in the capillary and leaving all other parameters constant, one expects to find an optimum yield for a certain pressure, which may depend on the harmonic order.

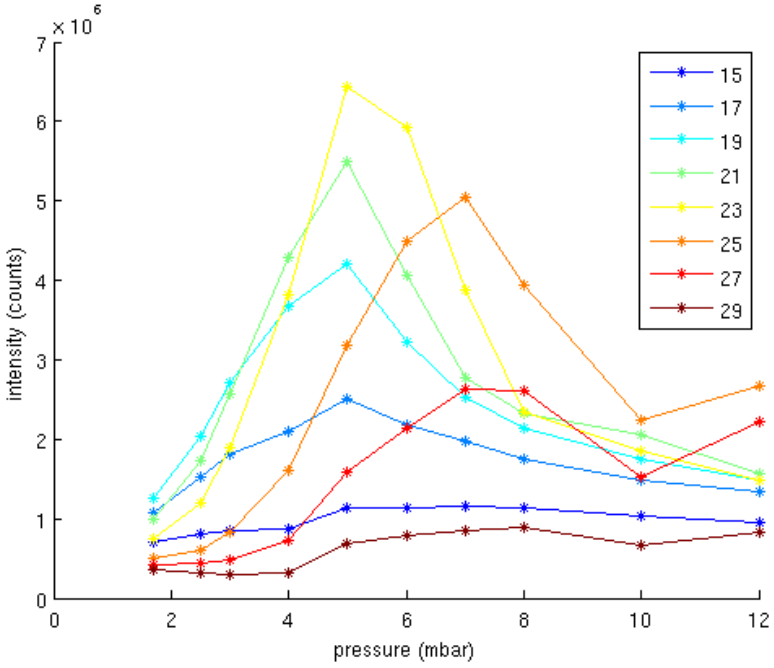

Figure 5.6: Pressure dependence of the harmonic yield.

This yield is shown in figure 5.6 as a function of the Argon pressure. The harmonic yield is averaged over 20 measurements with a 20 ms integration time. The pulse energy used is 7.5 mJ. The total yield is integrated over all harmonics peaks at a pressure of 5 mbar. At this pressure, the 17th to 23rd harmonic also produce a maximum yield. The 25th and 27th order give a maximum yield at a slightly higher pressure of about 7 to 8 mbar. Both the 15th and 29th harmonic show a near maximum yield over a broad pressure range. The increase in yield observed for the 25th and 27th harmonic for pressures above 10 mbar is not expected from the phase-matching argument given before.

This behavior may indicate more complicated dynamics for the generation of EUV radiation at higher pressures. This may also be coupled to the oscillations observed in the center of mass of the EUV pulses at the pressure of 12 mbar.

5.2 Testing of the evolutionary algorithm

The evolutionary algorithm (EA) is an important part of the control system for the EUV source; it performs automatic optimization of the pulse shaping to either enhance the yield or shift the wavelength of a particular harmonic. The behavior of the algorithm must be well understood in order to be able to use it effectively and to avoid long optimization times or even failure to optimize.

Several tests were performed to characterize the behavior of the EA. This was done by defining the fitness function as a mathematical function of the parameters given by the EA. The EA is tested in two scenarios. The first is the fitting of a sin(x) function by a polynomial, the second is maximizing a multi-dimensional sinc function.

5.2.1 Sine function fitting optimization

Fitting a sine function with a polynomial function is a very easy task for a computer. Mathematical software such as Matlab already provide the possibility to do a polynomial fit to any arbitrary array of data. The evolutionary algorithm can be tested easily for speed and accuracy as the end result is easily checked. The evolutionary algorithm is not optimized for this specific situation where an easily calculated solution is available but it provides a proof of principle nonetheless. The fitness F is defined as the summed mean squared error of the polynomial fitted to the sine function over the interval from - $2\pi \leq x \leq 2\pi$, where x is sampled at intervals of 0.01.

$$F = \sum_x \left(\sin(x) - \sum_n a(n) \cdot x^n \right)^2 \qquad 5.1$$

The constants $a(n)$, i.e. the coefficients of the orders of the polynomial, are the parameters of the individual.

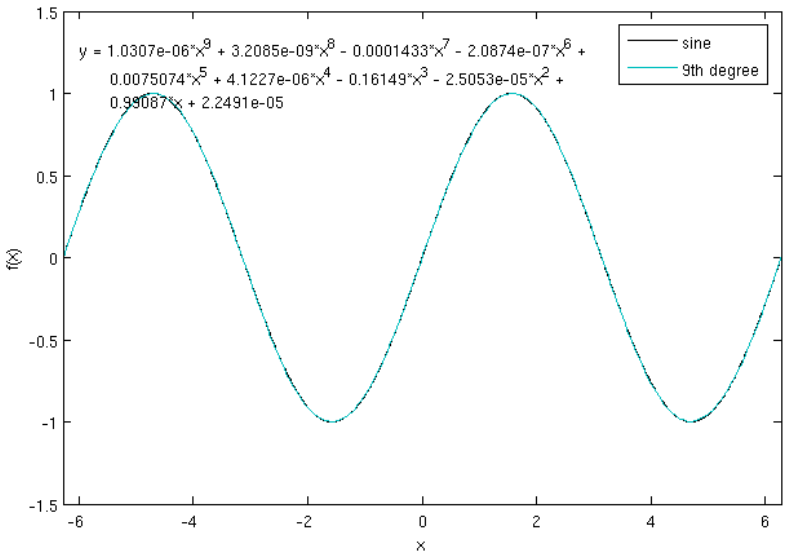

Figure 5.7: The data of the sine (black) and the fitted 9th order polynomial (blue) by the EA. p_n=20, p_f=10.

Figure 5.7 shows both the sin(x) function used as test function and the final 9th order polynomial produced by the evolutionary algorithm. The coefficients of this polynomial are compared to the coefficients that result from a least square polynomial fit of the same order to the sin(x) function. The coefficients are identical to at least the 5th decimal place. The optimization took more than 500 generations with a population size p_n of 20 to converge as can be seen in figure 5.8, which shows the fitness of each individual in a generation. The number of individuals of the population used to update the covariance matrix (p_f) was set to 10. In case of a HHG experiment involving reading out a spectrum remotely and programming the Dazzler remotely a testing a single individual can already take 2 seconds to load into the Dazzler and thus a generation consisting of 10 individuals takes minimally 20 seconds. Running the algorithm for 500 generations would take close to 3 hours However, the speed of convergence depends on many variables such as the number of parameters to optimize, the selectivity of the fitness function and the shape of the optimization landscape.

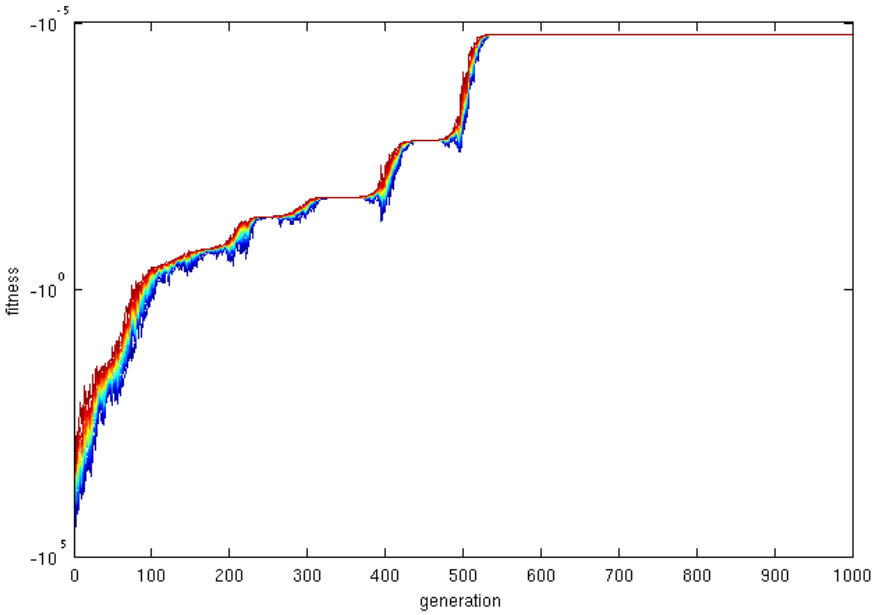

Figure 5.8: The fitness of each generation for a 9th degree polynomial including all orders. A rainbow colormap is applied for visualizing the fitness of individuals within the generations. p_n=20, p_f=10.

Figure 5.8 shows that the EA regularly seems to converge but after a number of generations again starts to improve the fitness. The source of this phenomenon is unknown but is important to understand as it can lead to the false conclusion that the algorithm has converged to the optimum.

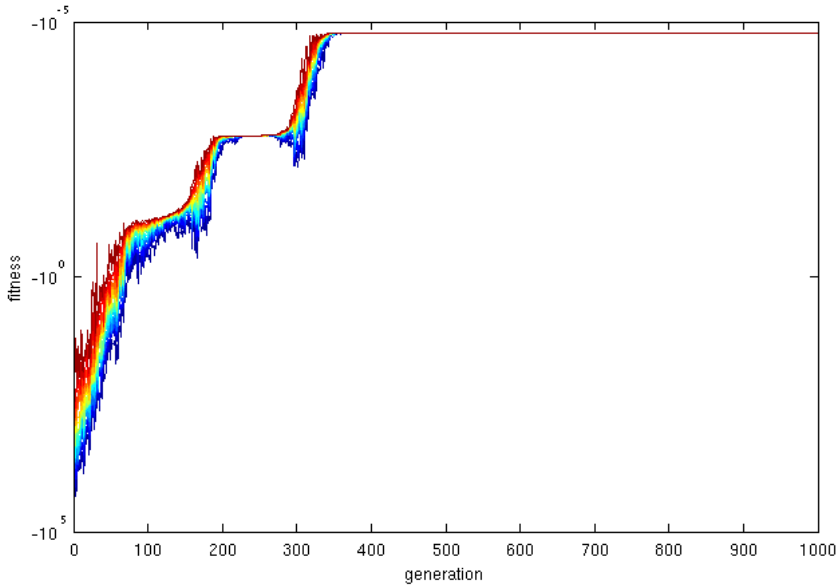

Figure 5.9: The fitness of each generation for fitting a sine with a 9th degree polynomial with only odd orders. A rainbow colormap is applied for visualizing the fitness of individuals within the generations. p_n=20, p_f=10.

In the optimization shown in figure 5.8 the EA tries to find the optimum coefficients of a 9th order polynomial to have the smallest possible difference with a sin(x) function. The EA was allowed to modify the coefficients of all orders, even the even ones. Since sin(x) is an odd function, the coefficients of the even terms should all be zero. If we use this prior knowledge about the function to optimize and set the coefficients of all even orders equal to zero, the optimization requires less generations as can be seen in figure 5.9, which shows the fitness of each individual in each generation. The optimization now only takes 350 generations to converge and the number of false convergences of the fitness function also dropped. Another parameter that influences the convergence of the EA is size of the parameter space that can be scanned by the EA. For the case shown in figure 5.9, the number of generations required before the EA converged only increase to 400 for a 10-fold increase of parameter space. Therefore, this optimization problem is only weekly dependent on the size of the parameter space. Note, the number of parameters is fixed, only the range of values that the parameters can take is increased.

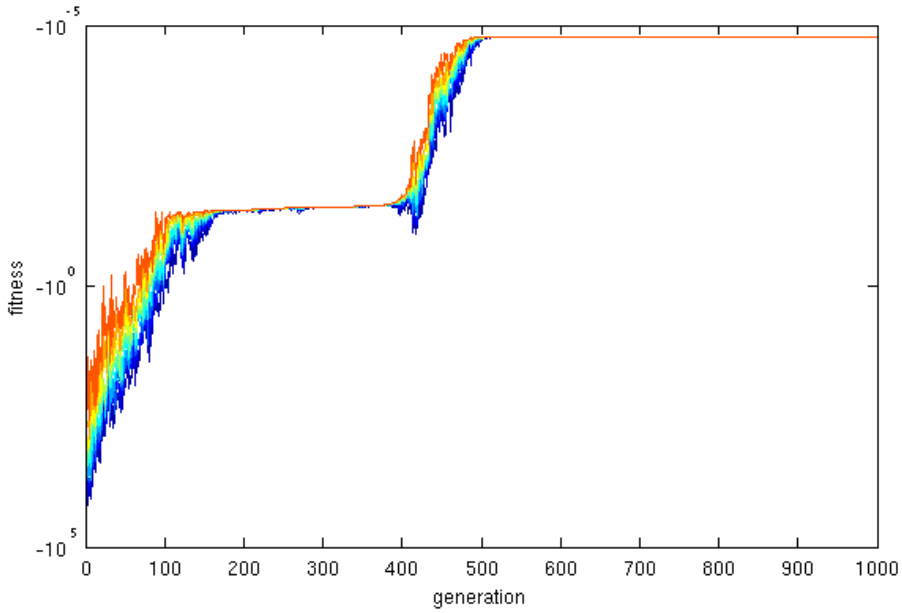

Figure 5.10: The fitness of each generation with a lowered population size of 10. A rainbow colormap is applied for visualizing the fitness of individuals within the generations. p_n=10, p_f=5.

The final parameter investigated is the population size. For the cases presented so far, the population size is 20. In figure 5.10 the population size is halved from 20 to 10. The fitness now converges after approximately 500 generations. Halving the population again hardly improved the results with a convergence after about 875 generations. At this point the population size equals the number of parameters to optimize. However, a too small population size can decreases the accuracy of the optimization because the initial spread of the population is limited.

5.2.2 Sinc(x) function optimization

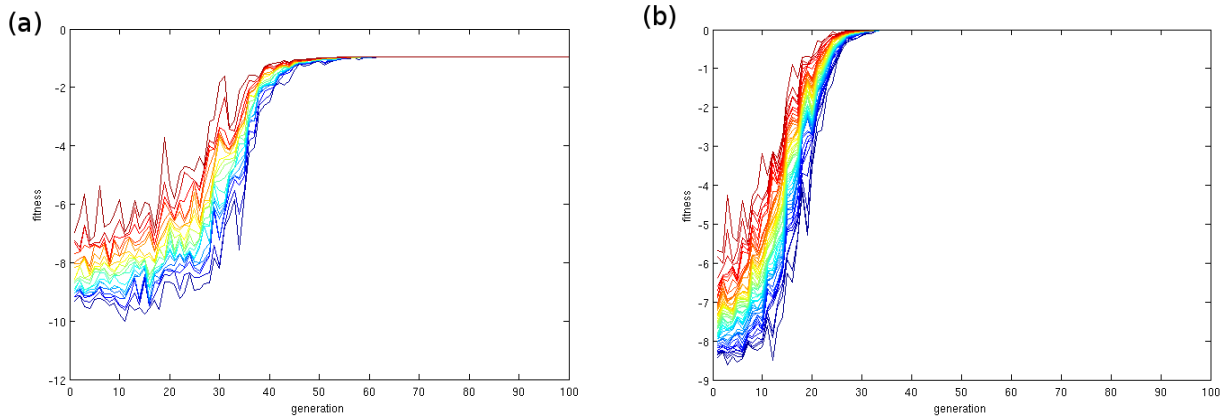

Figure 5.11: The fitness of each generation when optimizing for 8 sinc(x) functions. (a) p_n=20, p_f=10, (b) p_n=40, p_f=20. A rainbow colormap is applied for visualizing the fitness of individuals within the generations.

To test the EA in a different environment where the optimization landscape has multiple maximums, a sinc(x) was used and the particular fitness function used is defined as

$$F = \sum_n \operatorname{sinc}\left(x(n) - a(n)\right) - 1 \qquad 5.2$$

where *a(n)* are constants, and *x(n)* are the parameters. The optimum solution is when the optimization parameters x(n) are equal to the constants *a(n)*. At this point the fitness function equals 0. A sinc(*x*) function has many local maximums, posing a challenge for the evolutionary algorithm to find the absolute maximum. With *n=8* parameters and a population size of 20 the algorithm usually converged into a local maximum as seen in figure 5.11a. With a population size of 40 the algorithm found the global maximum reliably as seen in figure 5.11b. With a parameter landscape that contains many local maximums a large population size is more effective in finding the absolute maximum.

5.3 Pulse shaping using the oscillator

Second Harmonic Generation (SHG) is a straightforward non-linear process. The conversion to the second harmonic scales with the square of the incident electric field. Given a fixed pulse energy, the shortest possible duration of a pulse will have the highest intensity and thus the highest conversion efficiency. For a given bandwidth, the shortest pulse is the transform-limited pulse with a spectral phase that is flat over the bandwidth of the pulse. However, pulses rarely have a flat phase as propagation through a medium adds dispersion to the pulse which stretches the pulse and lowers the peak intensity of the pulse. This can pose a serious problem in many applications requiring high peak powers. It is therefore highly desirable to be able to measure and compensate for the dispersion of optical components added in the optical beam path.

5.3.1 Phase shaping

Using pulse shaping in combination with SHG provides a way to determine the dispersion at the point of the SHG crystal and compensate it using the Dazzler. The Dazzler can add an arbitrary spectral phase to the pulse. Only if this phase exactly compensates the spectral phase caused by the dispersion then the pulse at the SHG crystal is at its shortest and will have the highest conversion efficiency. This also opens a new way of measuring the dispersion of any material or even structures such as waveguides. First, the EA optimizes the SHG signal without the material present in the beam path. Then the EA again optimizes the SHG signal with the material present in the optical beam path. The additional dispersion added by the material should be compensated by the EA, and the difference in phase settings found by the EA is due to the material dispersion.

The compensation needed for the additional dispersion introduced by placing a component in the path of the optical beam (before the SHG crystal) can be found using a search algorithm. Two algorithms are used and compared. The first is the evolutionary algorithm and the second is a simple hill-climbing (HC) algorithm. The SHG process is a simple non-linear process with regard to the dispersion of an ultrashort pulse. The optimization landscape has no local maximums. This means that there is always one order of phase that can be changed to increase the SHG efficiency until the global maximum has been reached. The different orders of chirp are not fully decoupled. The fourth order chirp for example cannot be individually optimized to the value for a flat phase if a nonzero second order phase is present.

The evolutionary algorithm can find the optimal parameters quick and reliable in a noisy environment. The fitness is defined as the measured SHG power. The highest fitness corresponds to the highest SHG power. The SHG power is proportional to the conversion efficiency, which in turn is the highest for a pulse with a flat spectral phase (shortest pulse given the bandwidth).

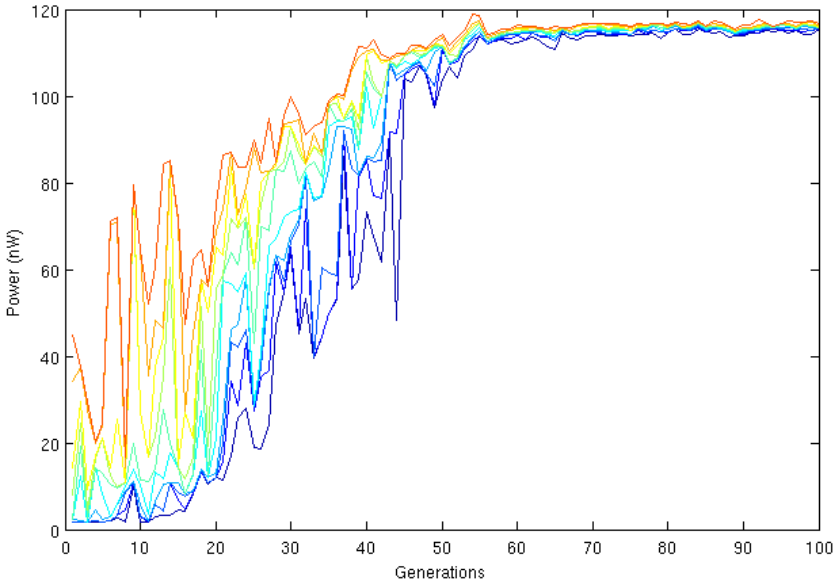

Figure 5.12: Optimization of the SHG efficiency by the evolutionary algorithm. The population size consists of 10 individuals with 4 parameters for the 1st through 4th order phase. A rainbow colormap is applied for visualizing the fitness of individuals within the generations.

Figure 5.12 shows the SHG power measured as the evolutionary algorithm optimizes the phase settings of the Dazzler. The first through fourth order phase are optimized within the parameter space given in table 1. The first order phase is only a delay and has no influence. Setting the first order phase to a fixed value can optimize the convergence speed but it was left in to analyze the behavior of a redundant parameter in a noisy shaping experiment. The optimum phase settings determined by the evolutionary algorithm are found in table 2. The optimization has been restarted to test if the EA converges to the same optimized values for the parameters. The evolutionary algorithm converged after 50 generations with a population size of 10.

Table 1: Parameter space of the EA for the SHG optimization

	1st order phase (fs)	2nd order phase (fs^2)	3rd order phase (fs^3)	4th order phase (fs^4)
minimum	4500	$-2.1 \cdot 10^4$	$-3.0 \cdot 10^4$	$-2.0 \cdot 10^5$
maximum	5500	$-1.5 \cdot 10^4$	$3.0 \cdot 10^4$	$2.0 \cdot 10^5$

A simple hill-climbing algorithm was also used to compare its performance against that of the evolutionary algorithm. The hill-climbing algorithm started with the self-compensating settings of the Dazzler and scans the second through fourth order phase separately over the given parameter space of table 1. The optimum for each phase is set as the starting point for searching for the next higher order phase. Consequently, the parameter space is reduced by a predetermined factor after optimization of each order of the phase. After each round, the averaging is increased in order to suppress the noise for an accurate determination of the optimal phase. With 4 rounds of 21 data points for 3 phase orders this gives 252 trial pulse shapes. The averaging doubles this to 504 trial pulse phases. This is approximately equal to the number of individuals (i.e. trial pulse shapes) the evolutionary algorithm needed to converge. The optimum phase settings found by the hill-climbing algorithm are given in table 2 as well. Here, the search algorithm is restarted 3 times to test if it converges to the same values. The HC search algorithm was again repeated 3 times, but now with a

5mm thick BK7 window placed in the beam path before the SHG crystal, to check if the dispersion of BK7 can be determined in this way.

Table 2: Phase constants found by the optimization algorithms for the highest SHG output. Each row present the optimal phase constants found in a measurement.

	fs^2	fs^3	fs^4
EA	-18866	-24637	27456
EA	-18897	-22572	-96331
HC (none)	-17971	-24624	-114895
HC (none)	-18082	-23513	-35265
HC (none)	-18082	-22773	5474
HC (BK7)	-18260	-24439	-118599
HC (BK7)	-18230	-24624	-177858
HC (BK7)	-18241	-25736	-174154

The measurements using the evolutionary algorithm and the hill-climbing algorithm were not taken at the same time. A change in the setup is the cause of the different phase constants found. The second order phase differs by approximately 800 fs^2, approximately the dispersion of the 14.1mm of BK7 that was present in the beam path when the EA was tested and was removed when the HC was tested. The difference between the measurement with and without the BK7 window show the possibility of determining the dispersion of the window. However, the accuracy is low. The reason for this can be found in figure 5.13, which shows the SHG power as a function of the added second order phase. The FWHM of the SHG power peak is more than 4 times wider than the dispersion added by the BK7 window. This ratio is an order of magnitude worse for the third order phase. This severely limits the accuracy of determining the dispersion of a material this way. In the case of a material the path length inside the material can be increased to increase precision but this also requires a high enough transmission of the material or structure under test to generate a detectable SHG signal.

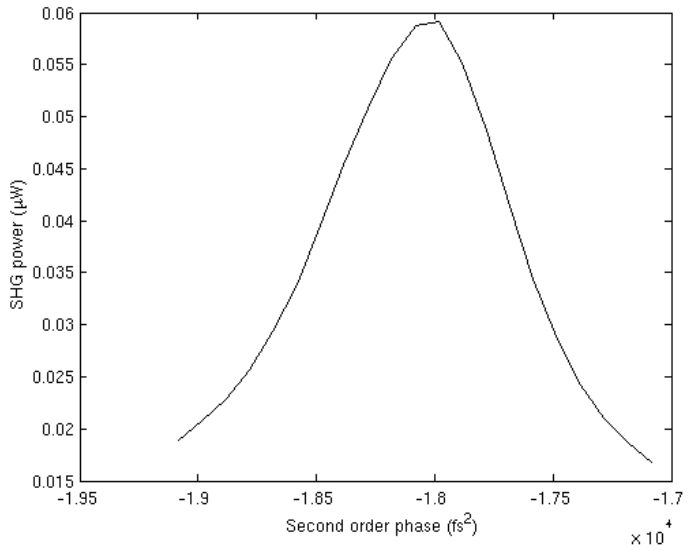

Figure 5.13: SHG power versus the second order phase added to the pulse.

5.3.2 Phase and amplitude shaping

Pulse shaping is not limited to only phase shaping but also allows amplitude shaping for complete control over the spectrum of the optical pulse. In this section we investigate the effect of adding amplitude shaping to the optimization of SHG as discussed in the previous section. The evolutionary algorithm is now allowed to optimize both the phase as well as the amplitude. Amplitude shaping can add more degrees of freedom to pulse shaping experiments and it can be used to compensate gain narrowing or a non-Gaussian oscillator spectrum.
Using amplitude shaping for SHG is useful as a test before using it in combination with the amplifier. Phase shaping can be safely done as the maximum added dispersion is negligible compared to the stretcher's dispersion. However, amplitude shaping can directly affect the pulse shape and duration inside the amplifier. Certain shaped pulses can damage the amplifier if the bandwidth of the seed pulse for the RGA is not sufficiently large or if the spectrum contains narrow spikes.

To optimize the amplitude of the spectrum, 5 wavelengths are defined for which the EA can optimize the amplitude. At each of the 5 wavelengths, the amplitude spectrum is flat over a range of 10 nm to avoid spikes in the spectrum. The 5 wavelengths are 25 nm apart and the center wavelength is at 800 nm. Outside this bandwidth of 135 nm the amplitude drops to zero. Inside the bandwidth, the amplitude spectrum is linearly interpolated to bridge the gaps, and the programmed spectrum is normalized by the Dazzler software. A fixed spectral hole is added into the amplitude spectrum to remove a peak in the oscillator spectrum. The hole has a relative depth of 20 % and is 15 nm wide centered around 795 nm. The resulting spectrum is shown in figure 5.14.

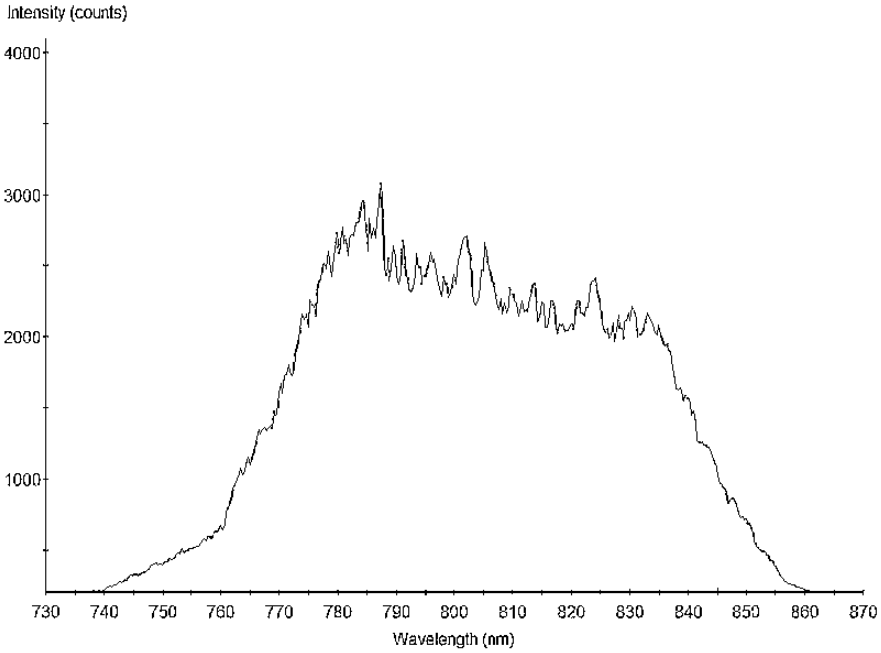

Figure 5.14: Oscillator spectrum after the Dazzler.

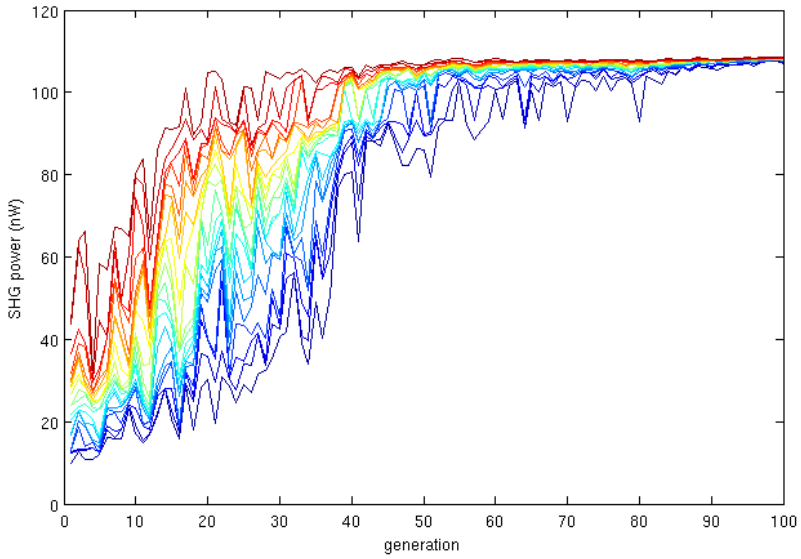

Figure 5.15: Optimization of the SHG efficiency by the evolutionary algorithm using both phase and amplitude shaping. The population size is 20 and 6 phase and 5 amplitude parameters are optimized. A rainbow colormap is applied for visualizing the fitness of individuals within the generations.

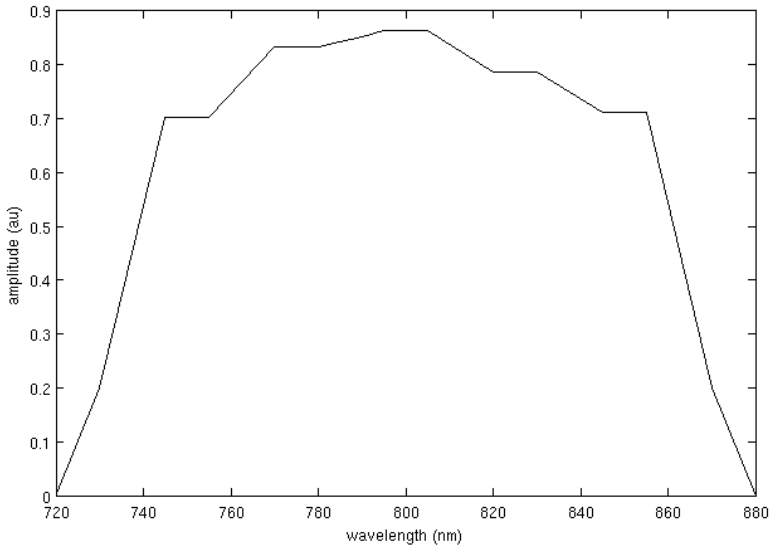

Figure 5.16: The optimized spectral amplitude transfer function found by the Dazzler.

Table 3: Parameter space used for shaping both amplitude and phase.

Phase	**fs2**	**fs3**	**fs4**	**fs5**	**fs6**	**fs7**
Maximum	$-1.1 \cdot 10^4$	$2 \cdot 10^4$	$1 \cdot 10^5$	$2 \cdot 10^6$	$4 \cdot 10^7$	$5 \cdot 10^8$
Minimum	$-2.0 \cdot 10^4$	$-2 \cdot 10^4$	$-1 \cdot 10^5$	$-2 \cdot 10^6$	$-4 \cdot 10^7$	$-5 \cdot 10^8$
Amplitude	**750**	**775**	**800**	**825**	**850**	
Maximum	1	1	1	1	1	
Minimum	0.5	0.5	0.5	0.5	0.5	

The second through seventh order phase were used as parameters for the phase shaping. The parameter space can be found in table 3. Together with the 5 parameters for the amplitude shaping the EA optimizes 11 parameters using a population of 20. Again the power of the SHG signal is used as fitness function and must be maximized by the EA. The fitness during the optimization is shown in figure 5.15. Unfortunately the third order phase parameter range was set to a too narrow range. The optimum phase found by the evolutionary algorithm is thus not accurate. The second order phase found matched the results in table 2 but the 4^{th} order phase optimum phase was found to be 46544 fs^4. This is significantly higher and may be the result of the incorrect 3^{rd} order phase, amplitude shaping or successful optimization of the higher order phases which were not optimized in the other measurements. The 5^{th} , 6^{th} and 7^{th} order phase were found to be $-5.6682 \cdot 10^5$ fs^5, $-3.2980 \cdot 10^6$ fs^6 and $-3.6216 \cdot 10^7$ fs^7, respectively. The optimized spectral amplitude transfer function is shown in figure 5.16. A flat amplitude transfer function would be expected as the Dazzler normalizes the programmed amplitude and a flat amplitude minimizes losses and thus maximizes the SHG signal.

5.4 Pulse shaping for HHG

In this section we discuss the results of applying pulse shaping to HHG. Different optimization goals can be set, for example the fitness function can be designed to selectively enhance the yield of a particular order of the harmonics regardless of the rest of the spectrum. Or, the fitness function can be defined to enhance a particular harmonic order while suppressing the other harmonics. Another possibility is to try to tune the wavelength of a particular harmonic order. All these goals are investigated in this section. Throughout this section, the EUV camera was set to an integration time of 20 ms, which means that the camera integrates 20 pulses for a single measurement of the spectrum. The EA was set to use a population size of 10.

5.4.1 Selective enhancement

The goal of selective enhancement is to enhance the intensity of a single harmonic with no regard of the intensity of other harmonics. The fitness function is defined as the sum of the counts C_h in an area of the camera's CCD sensor that correspond to a single harmonic. The evolutionary algorithm then looks for the optimum pulse shape that yields the highest intensity (counts) in the harmonic that falls in the given area. The fitness function can be written as follow:

$$F = C_h \tag{5.3}$$

Unfortunately, the measurements for selective enhancement were done when the drive laser was very unstable in power. For this reason, the results are averaged to increase the accuracy in determining the enhancement. All selective enhancement measurements were done with phase shaping only, using the 2^{nd} through 9^{th} order phase. The enhancement is determined in the following way. First the optimization using the EA is used. Directly after the optimum is obtained, a reference measurement is made using the self-compensating settings of the Dazzler. The enhancement is determined by the ratio of the yields obtained under these conditions.

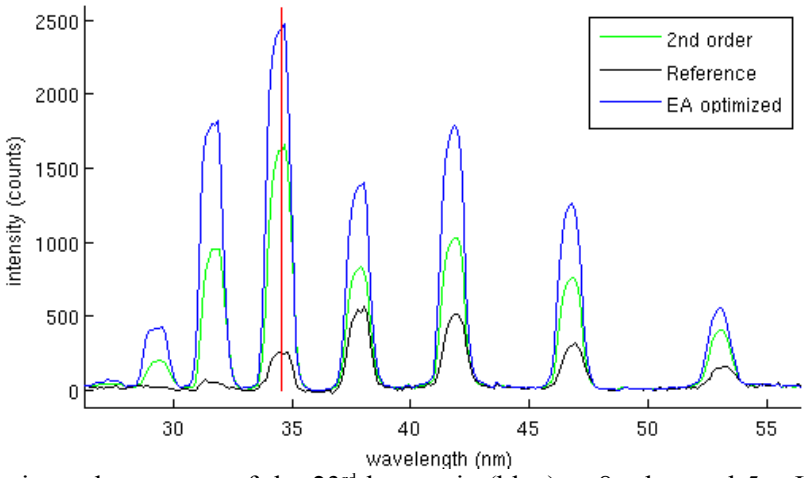

Figure 5.17 : Selective enhancement of the 23rd harmonic (blue) at 8 mbar and 5 mJ pulse energy. The 2nd through 9th order phase is optimized. Also plotted is the 2nd order parameter scan optimum (green) and reference (black).

The selective enhancement is done for different pressures. The result for a pressure of 8 mbar and a pulse energy of 5 mJ is plotted in figure 5.17. The complete last generation is averaged and plotted in blue with a red vertical marker to indicate the 23rd harmonic. A 2nd order phase parameter scan was performed directly after the optimization of which the optimum is plotted in green. The self-compensating settings of the Dazzler is taken as reference and is plotted in black.

The self-compensating setting of the Dazzler provides the shortest pulse at the laser exit. The enhancement of the 23rd harmonic when only optimizing the second order phase is already a factor 6.48. This may be the effect of compensating the dispersion of the capillary from the point of the incoupling to the point of the generation of the high harmonics. The EA improves this result by a factor 1.49, giving an enhancement of 9.65 compared to the reference.

5.4.2 Selective enhancement and suppression

In case of selective enhancement of a single harmonic order and at the same time suppressing the other orders, the fitness function definition contains both the harmonic that needs to be enhanced and the harmonic(s) that need to be suppressed. A simple definition of a fitness function favoring just one harmonic and suppressing all other is:

$$F = \frac{(C_h)^m}{C_0} \qquad 5.4$$

Where C_h the total counts is of the harmonic that should be optimized, C_0 the total counts of the zeroth diffraction order which is proportional to the total intensity. When the EA tries to maximize this fitness function this should result in a high C_h and a low C_0, meaning a large contrast between the harmonic that should be optimized and all other harmonics. The zeroth order of the grating can easily be taken as C_0. m is a number that determines the priority between enhancement and suppression and must be chosen carefully to obtain the wanted result. The fitness function used for the results in this section has m=1.1. This favors a large ratio between the harmonic and the total intensity without converging into background noise. Choosing a larger m favors a large increase of the total count rate C_0 even if this only increases the count rate of C_h slightly, which reduces the

contrast between C_h and C_0. A smaller m will favor a low count rate of C_h.

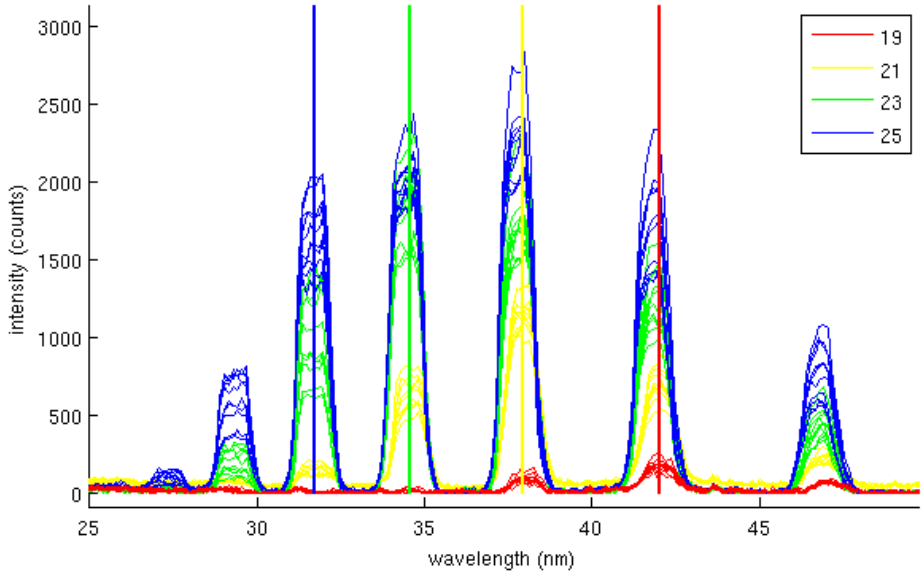

Figure 5.18: Selective enhancement and suppression for the 19th through 25th harmonic. The pressure used is 4 mbar and the pulse energy is 5 mJ and the 2nd through 7th order phase are optimized.

The result of the selective enhancement and suppression is plotted in figure 5.18. The optimization is done using a pressure of 4 mbar and a pulse energy of 5 mJ. The 2nd through 7th order phase is optimized. Each vertical marker represents a harmonic that was selectively enhanced. The marker and lines that are of the same color belong to each other, i.e., the yellow spectra are the results of trying to enhance the 21st harmonic (yellow marker). The full last population of the evolutionary algorithm is plotted to give an idea of the fluctuations after the shaping parameters have converged. For the 19th through 23rd harmonic the shaped pulse could make the selected harmonic the strongest of all harmonics present. Only for the 25th harmonic a different harmonic peaked, in this case the 21st. The optimization for the 19th harmonic is a good example of how the intensity is allowed to drop significantly to enhance one harmonic above the other.

The evolutionary algorithm did not succeed in creating a large enhancement in the yield of the favored harmonic while suppressing the yield for the other harmonics. The spectra obtained by optimizing the 25th harmonic have a higher intensity for every harmonic compared to the other optimization runs. This indicates that the evolutionary algorithm fails to enhance any harmonic and can only suppress harmonics in order to favor one harmonics above the other. Only the 2nd through 7th order phase has been used for the enhancement and suppression measurements. This was done to allow the evolutionary algorithm to converge with a reasonable time for the measurement to complete to avoid the long-term instabilities and alignment drift of the setup. However it may be necessary to use higher order phases as well for a better result. The extra degrees of freedom may open up new shaping possibilities

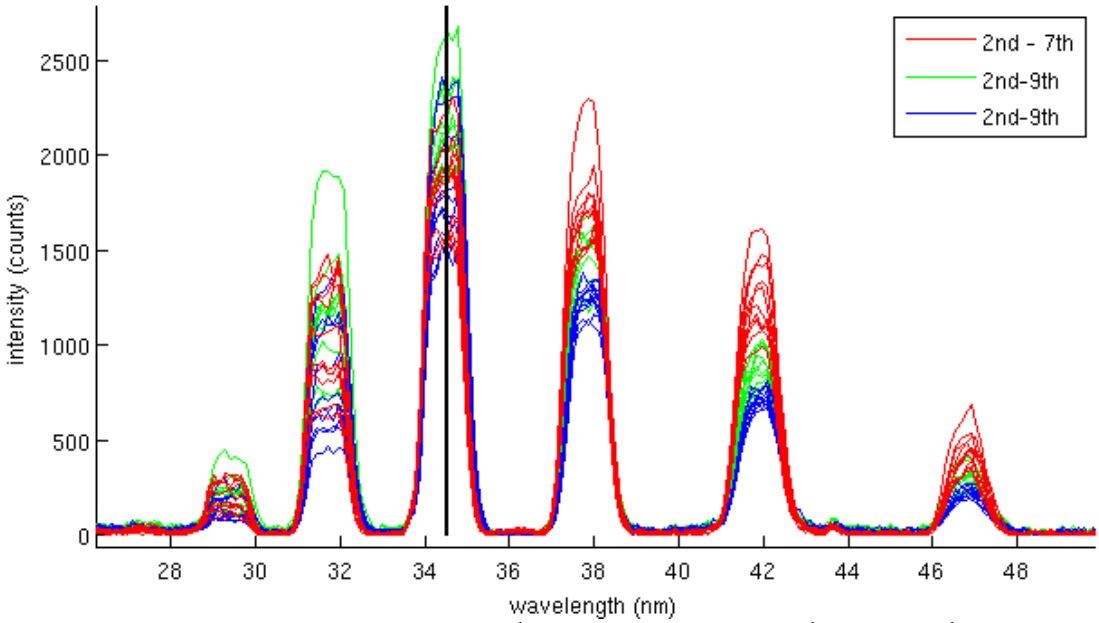

Figure 5.19: Shaping results optimizing the 23rd harmonic using the 2nd through 7th order spectral phase (single run) or the 2nd through 9th order (2 independent runs). The pressure used is 4 mbar, the pulse energy 5 mJ.

To investigate the effect of the higher order phase on the enhancement/suppression we have include the 8th and 9th order phase in a few runs were the 23rd harmonic is selectively enhanced. The results are shown in figure 5.19. Here 3 optimization runs are plotted, one where again the 2nd-7th order phase are used for shaping and two runs where the highest order in the phase has been increased to the 9th. Although some improvement can be seen, the overall effect is minor. The 23rd and higher harmonics grow slightly in intensity while the 21st and lower harmonics are more effectively suppressed. These results suggest that there may be some benefit to include even higher order phase in the optimization by the EA. However, this has not yet been investigated.

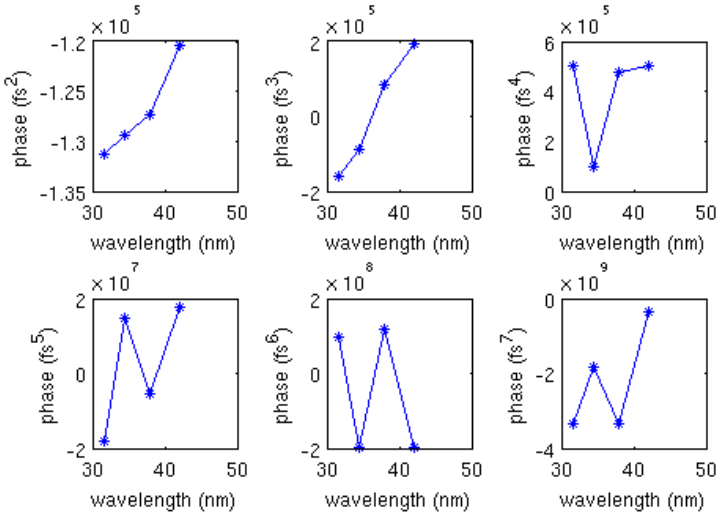

Figure 5.20: The phase constants determined by the evolutionary algorithms for optimization of a given wavelength.

The phase constants found by the evolutionary algorithm are shown in figure 5.20. With only selective enhancement of 4 different wavelengths, there is insufficient data to draw clear conclusions. However, the monotonic increase of the second and third order phase centered around the self-compensating setting of the Dazzler may indicate that these two orders plays a significant role in the tuning process.

5.4.3 Tuning

One of the key elements of creating a flexible EUV light source is tuning of the harmonics. The fitness function is identical to the fitness function used for the selective enhancement and suppressing so that measurements can be compared and reused. The interval that is used to sum the harmonic to be optimized is shifted to longer or shorter wavelengths. This favors a wavelength-shifted harmonic as the unshifted harmonics falls partly out of the spectral range that is optimized.

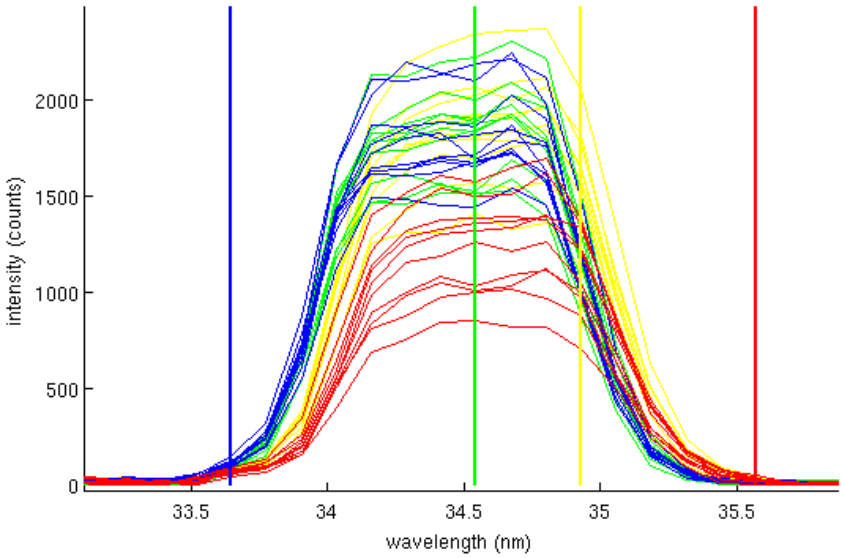

Figure 5.21: Tuning of the 23rd harmonic. The vertical lines indicate the center of the interval used in the fitness function. The pressure used is 4 mbar and the pulse energy is 5 mJ and the 2nd through 7th order phase are optimized.

Again we take the 23rd harmonic and try to either blue- or red shift its wavelength. The result can be found in figure 5.21. The vertical lines indicate the wavelength that the evolutionary algorithm tries to aim for. Again the color of the vertical marker and lines belong to each other. The full population of the converged generation for a particular wavelength is plotted to indicate the stability of the evolutionary algorithm. The center wavelength of the unshifted 23rd harmonic is 34.475 nm, corresponding to the green line. The actual tuning is small, if not absent. There is only a small difference visible at the wings of the peak. Calculating the center of mass of the harmonics for each shows that the wavelength shift is minimal. The resulting values are given in table 4. The total tuning range achieved for the 23rd harmonic is only 0.108 nm, corresponding to only 0.31% tuning of the central wavelength.

Table 4: target wavelength listed with results after optimization.

Target wavelength (nm)	33.647	34.545	34.929	35.570
Optimized wavelength (nm)	34.455	34.475	34.550	34.563

Only the 2nd through 7th order phase was used in the optimization process. As discussed in the previous section this may limit the shaping possibilities. No measurement was done using more degrees of freedom to give an indication of the shaping possibilities when also using the higher order phases.

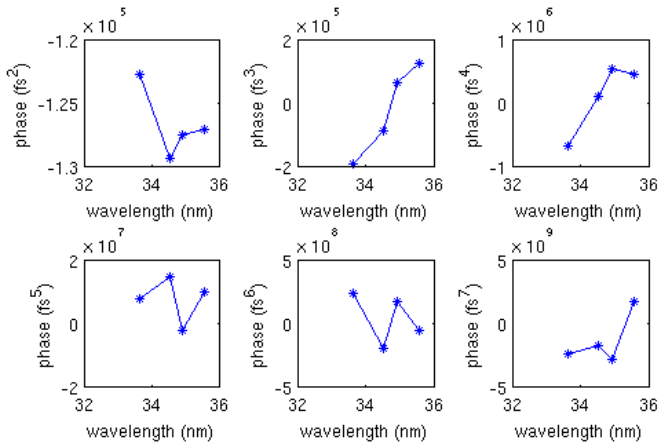

Figure 5.22: The phase constants determined by the evolutionary algorithms for optimization of a given wavelength.

The phase constants found by the evolutionary algorithm are shown in figure 5.22. With only selective enhancement of 4 different wavelengths, there is insufficient data to draw clear conclusions. However, the monotonic increase of the third order phase centered around the self-compensating setting of the Dazzler may indicate that the third order phase plays a significant role in the tuning process.

6
Conclusions and discussion

This thesis reports on high-harmonic generation in a large diameter capillary (500 μm instead of the usual 150 μm) filled with Argon and driven by a high-energy laser pulse of 35 fs in duration and pulse energy of about 5 mJ. The increase in capillary diameter and pulse energy of the drive laser required a complete rebuild of the experimental setup. To avoid self-phase modulation of the drive laser beam, it needs to propagate in vacuum. Furthermore, the filter that is required to separate the IR of the drive laser pulse from the EUV radiation needed to be placed about 9 m after the capillary to avoid damaging of the filter by the high intensity IR laser pulse. The overall setup proved to be reliable, and required no fine tuning over periods of several hours. This period was most often limited by the stability of the drive laser. Furthermore, available measurement time was limited due to a low up-time of the drive laser.

Nevertheless, high-harmonics are successfully generated with this setup. First, the generated EUV radiation is characterized. In the first measurements with the new set, the EUV camera was set to an integration time of 20 ms and therefore integrates over 20 subsequent pulses. Calculating the center of mass for the camera images showed a relative stable beam for low pressures and a significant oscillation in the x-coordinate at higher pressures. The camera images are slightly elliptical for pressures above 6 mbar with the larger axis along the y-direction.

Next, the spectrum was investigated. With the larger capillary diameter and pulse energy of about 7 mJ we were able to generate the 15^{th} to 29^{th} harmonic in Argon. The phase matching of the EUV generation process is investigated and the maximum yield for the 17^{th} to 23^{rd} order is obtained at a pressure of 5 mbar, while the other orders have a maximum yield at a slightly higher pressure of 7 to 8 mbar.

Finally, the effect of pulse shaping was investigated. A Dazzler was used to fully control the spectrum of the IR drive laser pulse by controlling both the amplitude and phase of the spectrum. The shaping is applied to the oscillator pulse before it is amplified in the regenerative amplifier and a subsequent single-pass amplifier.

For initial tests, the shaped oscillator pulse was directed out of the amplifier without being amplified. The evolutionary algorithm was tested by focusing the IR pulse into a SHG crystal and optimize for the second harmonic output. It was found that by inserting a piece of glass into the beam path (before the SHG crystal) and optimize again for maximum output of the second harmonic signal, the dispersion of the glass can be measured. The accuracy can be improved if the added dispersion (of a specific order) is a sufficiently large fraction of the width of the second harmonic output as a function of the same order of the spectral phase.

Shaping is then applied to optimizing the EUV output. The selective enhancement optimization shows a factor 9.65 increase in intensity in the 23^{rd} harmonic compared to the non-optimized case, which uses an unshaped, but fully compressed pulse as generated by the amplifier. This is comparable to the work of Bartels et. al.[3] which shows a factor 8 enhancement. The selective enhancement and suppression measurement did not show any enhancement and could only optimize the ratio between harmonics by suppressing the optimized harmonic less than other harmonics. The

tuning of the harmonics only showed a very small tuning range of 0.108 nm of the wavelength of the 23rd harmonic. This is small compared to the approximately 0.4 nm shift obtained by Froud et. al.[2].

7
Outlook

The HHG setup used for this thesis provides several possibilities to further investigate the high harmonic generation in a large diameter capillary and the effect of pulse shaping. This includes single shot measurements, expanding the pulse shaping options and investigating the influence of pressure and capillary dimensions on the pulse shaping.

Single shot measurements can reveal fluctuations on a shot-to-shot basis. This allows investigation of the correlation between the drive laser and the EUV beam. To allow single shot measurements, only a single EUV pulse may be incident on the camera per acquisition. The shutter in front of the spectrometer is not fast enough to open and close between pulses. A synchronized chopped wheel can reduce the repetition rate of the laser to 30 Hz, allowing single shot measurements, i.e., one EUV pulse is incident on the EUV camera per frame. In principle, one could reduce the repetition rate of the drive laser. However, stable operation of the laser requires operation at the design repetition rate of 1 kHz in order to avoid changes in thermal loading of the amplifier and subsequent changes in thermal lensing etc. Therefore the drive laser is kept running at 1 kHz repetition rate. The actual speed at with data can be collected is set by the speed at which the camera can transfer its data to a computer and is only 3 Hz.

The pulse shaping capabilities of the Dazzler have not been fully exploited. Phase shaping is done using only the 2^{nd} through 9^{th} order phase, leaving the possibility open to add higher-order phases. This allows a finer control over the pulse shape generated and may provide better capabilities of manipulating the HHG spectrum. Amplitude shaping can also provide a better control over the pulse shape. Amplitude shaping has not been applied with the HHG process in this thesis and can be done in future experiments. So far, only a limited number of fitness functions have been tested. It is worthwhile to investigate if other fitness functions with the same goal lead to the same optimized shaping of the pulse.

Finding the instabilities in the system may not provide exciting new capabilities but may improve the accuracy greatly and should still be investigated. Sources that produce vibrations, drive laser intensity fluctuations and gas flow instabilities may all have an effect on the stability of the high harmonics generated.

A more difficult study would be the analysis of the influence of the capillary dimensions on the shaping effectiveness. This requires measurements with different capillaries with varying dimensions, which is not easily done as this requires the venting of the capillary vacuum system section and realigning the capillary for each capillary change besides the manufacturing of multiple capillaries and change in focusing optics. Investigating the influence of the pressure on the pulse shaping however can be done without modifications. The larger diameter capillaries may also be more susceptible to excitation of higher order modes and these may either be detrimental or beneficial for the production of EUV radiation and this is worthwhile to investigate.

Appendix A

In the experimental setup used for this thesis the alignment is an important aspect. In the setup the total path length from the drive laser to the spectrometer is approximately 15 meters and passes many components which makes the alignment procedure not straightforward. Alignment must be done at a reduced power for safety and to avoid damaging components.

The coarse alignment is done only with the drive laser beam. The beam is first aligned using M1, M2 and M3 to the center of the focusing mirror M4. The focusing mirror is a fixed mirror and must be aligned to have an angle of incidence of 14 degrees. The reflection falls on M5 and is passed on to M6, both actuated mirrors. M4 and M5 are on a translation stage to shift he focus position along the beam path. The actuators and stage are initially in the middle of their adjustment range to allow the maximum travel in both directions after the vacuum system is closed and no other adjustments can be made by hand.

If the beamline itself is misaligned it should be realigned before proceeding. The alignment can be done using a HeNe laser for convenience. The beam is then aligned in the center of the beamline without the capillary or spectrometer installed. This is done with M6 and M7 to allow full control over the beam alignment. The drive laser is aligned to the end of the beamline without the capillary installed as the capillary would need realignment with every change in the drive laser beam alignment and vice versa. The drive laser beam after the capillary is also less powerful and more diverging which would make alignment even more difficult. The capillary is optimally aligned when the drive laser is normally incident on the capillary. As the drive laser is collinear with the beamline the capillary will also be collinear when properly aligned to the drive laser and thus be aligned to the beamline after the capillary.

Aligning the drive laser to the capillary or vice versa entrance can difficult as the capillary entrance is not easy visible when mounted. The following simple procedure can be used to realign the drive laser and the capillary to each other. In case of a misaligned capillary the capillary is moved with both translation stages and in case of a misaligned drive laser beam the drive laser beam is moved using M5 and M6 when the system is in vacuum and M6 and M7 when the system is at atmospheric pressure. When the drive laser hits the glass holder of the capillary holder this is easily distinguishable with an IR viewer. The position of the moved stage or mirror should be noted down. Movement should then be reversed in direction until the glass holder is hit by the driver laser again. The position of the moved stage or mirror should then be noted again. The average of both positions is the location of the capillary. This should be repeated for both x and y axis.

After installation of the capillary and spectrometer the EUV was visible on the spectrometer. The beam was centered on the spectrometer by moving the spectrometer itself several millimeters. For small movements this is easier to achieve than to adjust M5 and M6 and the 4 axis of the capillary adjustment to move the beam.

For large shifts of the beam on the EUV spectrometer it is best to keep the capillary entrance as a fixed point to avoid a large position shift of the whole capillary. The drive laser beam can be rotated around the capillary entrance by a combined movement of M5 and M6. The alignment starts by

determining the direction in which the EUV beam needs to be adjusted. By moving M6 to shift the drive laser beam in that direction and moving M5 in opposite direction to keep the focus at the capillary entrance the beam after the capillary will move in the intended direction. Each movement of M5 and M6 requires realignment of the capillary exit to keep the capillary collinear with the drive laser beam. Note that when using the XY stages to adjust the capillary that the movement of the capillary entrance and exit is not decoupled.

The shutter is placed approximately halfway the capillary and the spectrometer and can be adjusted perpendicular to the beamline. The shutter has an aperture of 6mm which, considering the divergence of the EUV beam, is enough not to clip the EUV beam. Clipping of the EUV beam by the shutter shows as typical diffraction rings in the measured beamprofile where the clipping of the aperture of the spectrometer itself is a sharply defined.

Appendix B

In this appendix the calculation for the angle of the focusing lens M4 is given as well as the calculation of the coupling efficiency for the drive laser beam size and focal length of M4 used.

Finding the q-parameter at the laser exit.

Lens used to determine the M^2:

$$f_{lens} \equiv 1000mm$$

The distance from the laser exit to the focusing lens:

$$z_{laser} \equiv 1070mm$$

Distance from the lens to the focus in the X-Z plane (i.e. horizontal plane):

$$z_{lensx} \equiv 99cm$$

Distance from the lens to the focus in the Y-Z plane (i.e. vertical plane):

$$z_{lensy} \equiv 101.6cm$$

The q-parameter at the focus are:

$$q_0 := \begin{pmatrix} i \cdot Z_{Rx} \\ i \cdot Z_{Ry} \end{pmatrix} = \begin{pmatrix} 19.796i \\ 11.879i \end{pmatrix} \cdot mm$$

$$z_{lens} := \begin{pmatrix} z_{lensx} \\ z_{lensy} \end{pmatrix}$$

To find the q-parameter at the laser exit we propagate back.
Just before the lens:

$$q_{lens1} := q_0 + z_{lens} = \begin{pmatrix} 0.99 + 0.02i \\ 1.016 + 0.012i \end{pmatrix} m$$

Just after the lens:

$$q_{lens2} := \begin{pmatrix} \dfrac{q_{lens1_0}}{\frac{-1}{f_{lens}} \cdot q_{lens1_0} + 1} \\ \dfrac{q_{lens1_1}}{\frac{-1}{f_{lens}} \cdot q_{lens1_1} + 1} \end{pmatrix} = \begin{pmatrix} 19.33 + 40.246i \\ -41.291 + 29.914i \end{pmatrix} m$$

At the laser exit:

$$q_{exit} := q_{lens2} + z_{laser} = \begin{pmatrix} 20.4 + 40.246i \\ -40.221 + 29.914i \end{pmatrix} m$$

At the laser exit the beam size and the radius of curvature are:

$$w_{exit} := \begin{bmatrix} M_x \cdot \left[\frac{\lambda}{\pi} \cdot \left(-\mathrm{Im}\left(\frac{1}{q_{exit_0}} \right) \right)^{-1} \right]^{\frac{1}{2}} \\ M_y \cdot \left[\frac{\lambda}{\pi} \cdot \left(-\mathrm{Im}\left(\frac{1}{q_{exit_1}} \right) \right)^{-1} \right]^{\frac{1}{2}} \end{bmatrix} = \begin{pmatrix} 4.092 \\ 4.694 \end{pmatrix} \cdot \mathrm{mm} \quad R_{exit} := \begin{pmatrix} \mathrm{Re}\left(\frac{1}{q_{exit_0}} \right)^{-1} \\ \mathrm{Re}\left(\frac{1}{q_{exit_1}} \right)^{-1} \end{pmatrix} = \begin{pmatrix} 99.797 \\ -62.469 \end{pmatrix} \mathrm{m}$$

Using a tilted spherical mirror to make the positions of the two focii equal.

The distance to the beam waist is:
(negative distance means that the waist is left to the exit plane)

$$z_0 := \mathrm{Re}(q_{exit}) = \begin{pmatrix} -20.4 \\ 40.221 \end{pmatrix} \mathrm{m}$$

The q-parameter at the waist is:

$$q_0 := q_{exit} - z_0 = \begin{pmatrix} 40.246\mathrm{i} \\ 29.914\mathrm{i} \end{pmatrix} \mathrm{m}$$

The size of the beam waist is:

$$w_0 := \begin{bmatrix} \left[\frac{\lambda}{\pi} \cdot \left(-\mathrm{Im}\left(\frac{1}{q_{0_0}} \right) \right)^{-1} \right]^{\frac{1}{2}} \\ \left[\frac{\lambda}{\pi} \cdot \left(-\mathrm{Im}\left(\frac{1}{q_{0_1}} \right) \right)^{-1} \right]^{\frac{1}{2}} \end{bmatrix} = \begin{pmatrix} 3.201 \\ 2.76 \end{pmatrix} \cdot \mathrm{mm}$$

The beam divergence angle is:

$$\theta_{laser} := \begin{pmatrix} \frac{-\lambda}{\pi \cdot w_{0_0}} \\ -\frac{\lambda}{\pi \cdot w_{0_1}} \end{pmatrix} = \begin{pmatrix} -4.558 \times 10^{-3} \\ -5.286 \times 10^{-3} \end{pmatrix} \cdot \mathrm{deg}$$

Radius of curvature of the spherical mirror:

$$R_{mirror} \equiv 5m$$

The focal lengths of the mirror in the tangential plane (X-Z) and sagittal plane (Y-Z) are:

$$f_{mirror} := \begin{pmatrix} \frac{R_{mirror}}{2 \cdot \cos(\theta)} \\ \frac{R_{mirror} \cdot \cos(\theta)}{2} \end{pmatrix}$$

The mirror is placed at a distance from the laser exit of:

$$z_{mirror} \equiv 2m$$

The q-parameter just before the mirror is:

$$q_{mirror1} := q_{exit} + z_{mirror} = \begin{pmatrix} -18.4 + 40.246i \\ 42.221 + 29.914i \end{pmatrix} m$$

The q just after the mirror is:

$$q_{mirror2} := \begin{pmatrix} \frac{q_{mirror1_0}}{\frac{-1}{f_{mirror_0}} \cdot q_{mirror1_0} + 1} \\ \frac{q_{mirror1_1}}{\frac{-1}{f_{mirror_1}} \cdot q_{mirror1_1} + 1} \end{pmatrix} = \begin{pmatrix} -2.511 + 0.13i \\ -2.518 + 0.071i \end{pmatrix} m$$

The q-parameter at a distance z from the mirror is:

$$q(z) := q_{mirror2} + z$$

The beam size at distance z from the mirror is given by:

$$w(z) := \begin{bmatrix} M_x \cdot \left[\frac{\lambda}{\pi} \cdot \left(-Im\left(\frac{1}{q(z)_0} \right) \right)^{-1} \right]^{\frac{1}{2}} \\ M_y \cdot \left[\frac{\lambda}{\pi} \cdot \left(-Im\left(\frac{1}{q(z)_1} \right) \right)^{-1} \right]^{\frac{1}{2}} \end{bmatrix}$$

We choose θ such that the real parts of q are made equal. In that case the two waists coincide.

The beam size at the focus is:

$$\min(W_x) = 207.397 \cdot \mu m$$

$$\min(W_y) = 136.358 \cdot \mu m$$

The position of the focus is found using the root function of Mathcad:

$$f_x(z) := w_x(z) - \min(W_x) \qquad f_y(z) := w_y(z) - \min(W_y)$$

We made the two positions equal by adjusting the angle of incidence. We found:

$$\theta = 14.2 \cdot deg$$

Matched Spot Size for capillary mode coupling.

Focal length of focusing mirror:

$$f := 2500 \cdot 10^{-3} \quad m$$

Beam radius ($1/e^2$) of drive laser:

$$d := 4.429 \times 10^{-3} \quad m$$

Capillary inner diameter:

$$aa := 508 \quad \mu m$$

Wavelength of drive laser:

$$\lambda := 800 \cdot 10^{-9} \quad m$$

Focal spot size:

$$w_o := \lambda \cdot \frac{f}{\pi d} \qquad w_o = 1.437 \times 10^{-4} \quad m$$

Capillary radius:

$$a := \frac{aa}{2} \quad \mu m$$

*m*th root of Zero order Bessel Function:

$$u_m := 2.405$$

Coupling efficiency:

$$n_m(w) := \frac{\left[\int_0^a \left[e^{\left[\frac{-r^2}{(w)^2}\right]}\right] J0\left(u_m \cdot \frac{r}{a}\right) r\, dr\right]^2}{\left[\left[\int_0^\infty e^{\left(\frac{-2r^2}{w^2}\right)} \cdot r\, dr\right]\right] \cdot \left[\int_0^a \left(J0\left(u_m \cdot \frac{r}{a}\right)\right)^2 \cdot r\, dr\right]}$$

We find: $n_m(w) = 0.961$

Acknowledgments

The research described in this thesis marks the end of my study for master in Applied Physics here at the Twente University. It concludes a 6.5 year study in what I consider the most awesome field of science. In the first year of my study my interest was already drawn to lasers. Via Fred van Goor who gave the lectures of the introductory optics course I first heard about the LPNO group. My fascination with the laser wake-field acceleration setup contributed to my choice to do my Bachelor assignment at the LPNO group. With Fred van Goor as my supervisor I worked on an inverted field autocorrelator for ultrashort pulses and greatly enjoyed the work and my stay in the LPNO group.
Some years later I returned to the LPNO group for my master assignment. Again I started working in the field of ultrashort pulses, this time on high harmonic generation. Much to my pleasure this involved building a huge experimental setup with many practical challenges. I accepted the delays and difficulties unavoidably associated with such a setup as part of the job. In general I can look back to a very educational experience and I am thankful I can conclude my master with the research presented in this thesis.

I would like to thank the people I have worked with and everybody who helped me during my time here at the LPNO group. First of all I'd like to thank Peter van der Slot for supervising me and for the hard work put into revising this thesis. Without his help this thesis would have a very short coherence length. I'd then like to thank Jean Goh for the teamwork, we shared the fun and frustrations of building, aligning and maintaining the large experimental setup. I also want to thank Gerard Oude Meijers for his help with the building of the vacuum system and his very useful insight in keeping it in optimum condition. Thanks also to Bert Bastiaens for the fruitful discussions and the practical assistance in various parts of the setup. I also want to thank Fred van Goor for his expertise and help on the complicated laser system. I have learned much about femtosecond laser systems from you and I very much enjoyed the more than lunch break long discussions about various laser related subjects. I'd like to thank Klaus Boller for the opportunities he has given me to do various assignments and to perform my master research in the LPNO group. I also want to thank Herman Offerhaus for joining the graduation committee. Finally a big thanks to the whole LPNO group for all the fun we had and the various activities we did together. I really enjoyed being part of this group and I hope to see many of you in the future.

References

[1] Chapman, Henry N., et al. "Femtosecond diffractive imaging with a soft-X-ray free-electron laser." *Nature Physics* 2.12 (2006): 839-843.

[2] Froud, C. , Brocklesby, W.S. , Rogers, E. , Hanna, D.C. , Praeger, M. , de Paula, A.M. , Baumberg, J.J. , Frey, J.G., Quantum Electronics Conference, 2005. EQEC '05. European

[3] Bartels, Randy, et al. "Shaped-pulse optimization of coherent emission of high-harmonic soft X-rays." *Nature* 406.6792 (2000): 164-166.

[4] Reitze, David H., et al. "Enhancement of high-order harmonic generation at tuned wavelengths through adaptive control." *Optics letters* 29.1 (2004): 86-88.

[5] Ogilvie, J. P., Débarre, D., Solinas, X., Martin, J. L., Beaurepaire, E., & Joffre, M. (2006). Use of coherent control for selective two-photon fluorescence microscopy in live organisms. *Opt. Express*, *14*(2), 759-766.

[6] Itakura, R., Yamanouchi, K., & Kannari, F. (2010). Selective bond breaking in dissociative ionization of ethanol induced by tailored intense laser fields. *Advances in multi-photon processes and spectroscopy, v. 19*, *19*, 93.

[7] Shapiro, Moshe, and Paul Brumer. "Principles of the quantum control of molecular processes." *Principles of the Quantum Control of Molecular Processes, by Moshe Shapiro, Paul Brumer, pp. 250. ISBN 0-471-24184-9. Wiley-VCH, February 2003.* 1 (2003).

[8] Meshulach, Doron, and Yaron Silberberg. "Coherent quantum control of two-photon transitions by a femtosecond laser pulse." *Nature* 396.6708 (1998): 239-242.

[9] Meshulach, Doron, and Yaron Silberberg. "Coherent quantum control of multiphoton transitions by shaped ultrashort optical pulses." *Physical Review A* 60.2 (1999): 1287.

[10] C. Winterfeldt. Generation and control of high-harmonic radiation. PhD thesis, Universität Würzburg, 2006.

[11] Emily Gibson, Ivan Christov, Margaret M. Murnane, and Henry C. Kapteyn. Femtosecond Optical Frequency Comb: Principle, Operation, and Application, chapter 11, Quantum control of high harmonic generation. Springer US, 2005.

[12] He, Lixin, et al. "Wavelength dependence of high-order-harmonic yield in inhomogeneous fields." *Physical Review A* 88.5 (2013): 053404.

[13] Perry, Michael D., and John K. Crane. "High-order harmonic emission from mixed fields." *Physical Review A* 48.6 (1993): R4051.

[14] T. Brabec and F. Krausz, Intense few-cycle laser fields: Frontiers of nonlinear optics, Rev. Mod. Phys. 72, 545 (2000).

[15] Nuernberger, Patrick, et al. "Femtosecond quantum control of molecular dynamics in the condensed phase." *Physical Chemistry Chemical Physics* 9.20 (2007): 2470-2497.

[16] Bock, Martin, et al. "Spectral and temporal response of liquid-crystal-on-silicon spatial light modulators." *Applied Physics Letters* 92.15 (2008): 151105-151105.

[17] http://en.wikipedia.org/wiki/File:AOPDF_principle.png, copy made on 04/12/2013

[18] R. Fanciulli, L. Willmes, J. Savolainen, P. van der Walle, T. B¨ack, and J. L. Herek, “Evolution strategies for laser pulse compression,” Lecture Notes in Computer Science 4926, 219–230 (2008).

[19] Bas-Jan Zandt. Towards efficient High Harmonic Generation in the few nm wavelength regime . Master’s thesis, University of Twente, 2009.

[20] Braun, A., et al. "Self-channeling of high-peak-power femtosecond laser pulses in air." *Optics letters* 20.1 (1995): 73-75.

[21] Hill, S. B., et al. "Measuring the EUV-induced contamination rates of TiO2-capped multilayer optics by anticipated production-environment hydrocarbons." *SPIE Advanced Lithography*. International Society for Optics and Photonics, 2009.